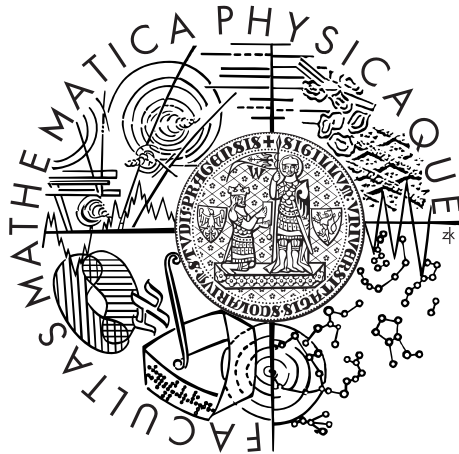Univerzita Karlova v Praze

Matematicko-fyzikální fakulta

DIPLOMOVÁ PRÁCE

Bc. Pavol Štefko

Studium tvrdých procesů ve srážkách těžkých iontů na detektoru ATLAS

Ústav částicové a jaderné fyziky

Vedoucí diplomové práce: Mgr. Martin Spousta, Ph.D.

Studijní program: Fyzika

Studijní obor: Jaderná a subjaderná fyzika

Praha 2015

Charles University in Prague

Faculty of Mathematics and Physics

MASTER THESIS

Bc. Pavol Štefko

Study of hard processes in heavy ion collisions at ATLAS

Institute of Particle and Nuclear physics

Supervisor of the master thesis: Mgr. Martin Spousta, Ph.D.

Study programme: Physics

Specialization: Nuclear and Subnuclear Physics

Prague 2015

Acknowledgments

I declare that I carried out this master thesis independently, and only with the cited sources, literature and other professional sources.

I understand that my work relates to the rights and obligations under the Act No. 121/2000 Coll., the Copyright Act, as amended, in particular the fact that the Charles University in Prague has the right to conclude a license agreement on the use of this work as a school work pursuant to Section 60 paragraph 1 of the Copyright Act.

In Prague, date 7.5.2015   signature of the author

Název práce: Studium tvrdých procesů ve srážkách těžkých iontů na detektoru ATLAS

Autor: Bc. Pavol Štefko

Katedra: Ústav částicové a jaderné fyziky

Vedoucí bakalářské práce: Mgr. Martin Spousta, Ph.D.

Abstrakt: Bola študovaná produkcia jetov v zrážkach jadier olova pri ťažiskovej energii na jeden nukleón 2,76 TeV použitím detektoru ATLAS na urýchľovači LHC. Predpokladá sa, že interakcie partónov s veľkou priečnou hybnosťou s horúcou, hustou hmotou produkovanou pri týchto ultrarelativistických kolíziách spôsobujú stratu energie produkovaných jetov (tzv. tlmenie jetov). Táto práca prezentuje výsledky analýzy jetov vykonanej na dátach získaných počas runu s ťažkými iónmi na LHC v roku 2011 a taktiež na referenčnom PYTHIA Monte Carle. Jety boli rekonštruované použitím anti-k_t algoritmu a študované ako funkcia centrality kolízie a dvojjetovej energetickej nerovnováhy. S rastúcou centralitou bol pozorovaný nárast asymetrie jetov, v súlade s teóriou tlmenia jetov. Ďalej potom štúdium dráh nabitých častíc indikuje nárast počtu častíc s malou priečnou hybnosťou v jete, ktorý podstúpil silné potlačenie.

Kľúčové slová: tlmenie jetov, zrážky ťažkých jadier, ATLAS, Veľký Hadrónový Urýchľovač

Title: Study of hard processes in heavy ion collisions at ATLAS

Author: Bc. Pavol Štefko

Department: Institute of Particle and Nuclear physics

Supervisor: Mgr. Martin Spousta, Ph.D.

Abstract: Jet production in PbPb collisions at a per-nucleon center-of-mass energy of 2.76 TeV has been studied using the ATLAS detector at the LHC. Interactions between the high-p_T partons and the hot, dense medium, produced in these ultrarelativistic collisions, are expected to cause the loss of the jet energy (jet quenching). This thesis presents results of the jet analysis done on the data taken during the 2011 heavy-ion run at the LHC as well as PYTHIA Monte Carlo reference. Jets are reconstructed using the anti-k_t jet clustering algorithm and studied as a function of collision centrality and dijet energy imbalance. With increasing centrality, dijets are observed to be increasingly asymmetric, consistent with the theory of jet quenching. The study of charged particle tracks indicates the increase of the low-p_T tracks in the strongly quenched jets.

Keywords: jet quenching, heavy-ion collisions, ATLAS, Large Hadron Collider

Contents

Introduction

The subject of this thesis is a study of experimental measurements of jets in ultra-relativistic heavy-ion collisions and the phenomenon of jet quenching. Collisions of the heavy ions at these energies are expected to produce a dense medium of extremely high temperatures in order of trillion kelvins, as predicted from lattice Quantum Chromodynamics (QCD) calculations. This phase of matter consists of deconfined quarks and gluons as degrees of freedom and it is, therefore, accordingly called a quark-gluon plasma (QGP). QGP allows to test QCD in the limit of extreme temperatures and densities. Furthermore, it is believed that the QGP existed at the very early stages of our universe. Therefore the study of the properties of this phase may provide a critical insight into the dynamics of this era.

Attempts to create and study the QGP have been previously made at CERN's (The European Organization for Nuclear Research) Super Proton Synchrotron (SPS) in the 1980s and 1990s, later at the Relativistic Heavy Ion Collider (RHIC) at the Brookhaven National Laboratory on Long Island (NY, USA) and most recently in PbPb collisions at CERN's Large Hadron Collider (LHC).

High transferred momentum interactions of quarks and gluons in colliding beams are known to produce highly collimated clusters of hadrons and other particles produced by hadronization referred to as jets. Jets have long been thought to interact with the ambient plasma and, therefore, to serve as probes of the QCD matter created in the collisions. The process by which a quark or gluon loses energy in a medium of high color charge density is called jet quenching.

Of special interest are the "dijets" consisting of the two energetic jets. These two jets are expected to have on average comparable energies and are also expected to be ejected in back-to-back geometry (i.e., having azimuthal difference close to π). However, the strong interactions of quarks and gluons inside the hot medium can significantly modify the dijet energy balance between the two most energetic jets. It is therefore important to study these modifications of dijet properties, since they can provide useful information about the properties of the QCD medium formed in the collisions.

The analysis in this work was made using the data from heavy-ion collisions at nucleon-nucleon center-of-mass energy 2.76 TeV, which were collected by the ATLAS (A Toroidal LHC ApparatuS) detector in 2011. These results were further compared to those in PYTHIA Monte Carlo and those performed by CMS

Collaboration.

This thesis is organized as follows: Chapter 1 provides the theoretical background, introducing the theory of strong interaction, the concept of jets and jet algorithms, and the concept of quark gluon plasma. These concepts are introduced in order to motivate the use of heavy-ion collisions as an experimental tool to study the strong interaction. The motivation for this work follows in Chapter 2. Chapter 3 contains the descriptions of the ATLAS detector and the LHC, which provided the measurement presented in this work. Information about basic observables and various cuts and corrections used in the analysis is discussed in Chapter 4. The results of the experimental analysis are presented in Chapter 5 with the conclusions following in the last chapter.

Chapter 1

Strong Interaction and Heavy Ion Collisions

This chapter provides a short overview of the theory of strong interactions called the Quantum Chromodynamics. We shall outline the basic concepts of this theory, introduce the concept of jets and jet algorithms and discuss the concept of quark-gluon plasma. The quark-gluon plasma (QGP) is the main object of study in ultrarelativistic heavy ion physics. It is an unexplored state of matter in which the relevant degrees of freedom are not hadrons, but quarks and gluons. It is believed that the QGP is one of the primordial forms of matter, which existed in the very early stages of our universe, only few microseconds after the Big Bang [1].

1.1 General Concepts of Quantum Chromodynamics

Quarks are one of the smallest known subdivisions of matter that have various intrinsic properties, including electric charge, color charge, mass, spin, and flavor. They combine to form composite particles called hadrons, either baryons (consisting of three quarks) or mesons (consisting of one quark and one antiquark). The theory explaining the interactions among quarks is called the Quantum Chromodynamics (QCD). Following text is based on classical literature of particle physics [2, 3].

QCD is the Yang-Mills theory of quantum field with a non-Abelian gauge symmetry group SU(3), with Lagrangian density given by

$$\mathcal{L}_{\text{QCD}} = -\frac{1}{4} F_{\mu\nu}^C F^{C\mu\nu} + \sum_f \bar{\psi}_f (i\gamma^\mu D_\mu - m_f) \psi_f, \tag{1.1}$$

with the f index denoting the flavor of quark of "bare" mass m_f and Dirac spinor ψ_f, C is the color index running from 1 to 8 (corresponding to the dimensionality of SU(3)), and γ_μ are the four Dirac matrices. The fermion fields

have an additional color index that runs from 1 to $N_C = 3$ but is suppressed in notation for brevity. The field strength tensor $F^C_{\mu\nu}$ is expressed in terms of eight gauge gluon fields A^C_μ via

$$F^A_{\mu\nu} = \partial_\mu A^A_\nu - \partial_\nu A^A_\mu - g f_{ABC} A^B_\mu A^C_\nu, \qquad (1.2)$$

where g is the QCD coupling constant (sometimes referred to as $\alpha_s = g^2/4\pi$) and f_{ABC} are the structure constants of the SU(3) group. The covariant derivative appearing in (1.1) is defined as

$$D_\mu = \partial_\mu - ig \sum_C t^C A^C_\mu. \qquad (1.3)$$

Here t^C are generators of the gauge group represented by eight 3×3 matrices satisfying the Lie algebra

$$[t_A, t_B] = i f_{ABC} t_C. \qquad (1.4)$$

The covariant derivative ensures that the Lagrangian is invariant under SU(3) gauge transformations

$$\psi_f \to U\psi_f = e^{i\epsilon}\psi_f, \qquad \bar{\psi}_f \to \bar{\psi}_f U^\dagger = \bar{\psi}_f e^{-i\epsilon}, \qquad (1.5a)$$

$$A_\mu \to A_\mu + \frac{i}{g}\partial_\mu\epsilon. \qquad (1.5b)$$

Writing out the Lagrangian (1.1) explicitly using relations (1.2) and (1.3) we can separate the $\mathcal{L}_{\text{QCD}}$ into a free and interaction part: $\mathcal{L}_{\text{QCD}} = \mathcal{L}_0 + \mathcal{L}_{\text{int}}$. The interaction part can be written schematically as

$$\mathcal{L}_{\text{int}} = gA\bar{\psi}\psi + gAA\partial A + g^2 AAAA. \qquad (1.6)$$

The first term is obviously a coupling, of strength g, between the quarks and massless, spin-1 gauge fields representing gluons, the second term is apparently a three gauge boson coupling having strength g and the third term is a four gauge boson coupling proportional to g^2. The Feynman diagrams corresponding to these couplings are displayed on Figure 1.1.
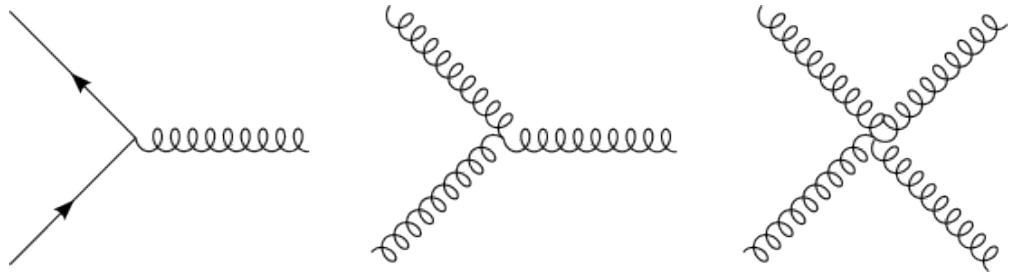

Figure 1.1: Couplings corresponding to the tree terms in the QCD $\mathcal{L}_{\text{int}}$. In addition to the gauge coupling present also in quantum electrodynamics (shown on the left) the non-Abelian structure of the theory allows for coupling between the gauge fields themselves (middle and right).

Like in the quantum field theory describing the electromagnetism (EM), where the carriers of the EM force (gauge bosons) are photons, the interactions of QCD are realized by the exchanging of gluons, and the accompanying force is called the strong nuclear force. Quarks and gluons are collectively called *partons*. Quarks are the only known elementary particles in the standard model that engage in all four fundamental forces of contemporary physics (electromagnetism, gravitation, strong interaction, and weak interaction) [4].

The main difference between QED, which is an abelian gauge field theory, and QCD, is that the electrodynamical gauge bosons (photons) do not carry the charge that they couple to and, hence, do not interact with each other. This is, as can be seen from Figure 1.1, not the case in QCD. Here, the gluons do carry the color charge and thus couple not only to fermions, but also to other gluons. This non-abelian structure of QCD leads to two surprising phenomena, namely *color confinement* and *asymptotic freedom*.

As already mentioned, fields and physical quantities appearing in the QCD Lagrangian in Equation (1.1) are "bare". Generally, when doing a perturbative expansion of an observable, Lagrangian in this form introduces contributions from quantum loops. These loops describe creation and subsequent annihilation of virtual particles and are particularly important at large momentum scale Q^2 where they cause ultraviolet (UV) divergencies. These divergencies can be eliminated via a redefinition of fields and other parameters of Lagrangian (1.1), a process called *renormalization*. During this process, Lagrangian is separated into a physical part and a counter-term part which is chosen to exactly cancel divergencies in observables order by order. As a direct consequence of this, the original coupling constant g (or equivalently, α_s) now depends on the momentum scale Q^2.

This so-called "running" of coupling constant is encoded in following renormalization group equation:

$$\frac{\partial \alpha_s}{\log Q^2} \equiv \beta(\alpha_s) = -\alpha_s^2(\beta_0 + \alpha_s\beta_1 + \ldots), \qquad (1.7)$$

where $\beta(\alpha_s)$ represents so-called β function which can be expanded. Once we know this function at a given order of the perturbative expansion we can solve the equation (1.7) to obtain coupling at scale Q^2 given the coupling at lower scale μ^2, sometimes called renormalization scale. At the lowest order we obtain:

$$\alpha_s(Q^2) = \frac{\alpha_s(\mu^2)}{1 + \alpha_s(Q^2)\beta_0/4\pi \log(Q^2/\mu^2)}. \qquad (1.8)$$

Equation (1.8) describes how the coupling "runs" from μ^2 to Q^2. The one loop coefficient β_0 of the β-function was first calculated by David Gross, David Politzer and Frank Wilczek in 1973 [5, 6]. It is equal to:

$$\beta_0 = 11 - \frac{2}{3}N_f, \qquad (1.9)$$

where N_f is the number of fermion flavors. In our universe this number is $N_f = 6$ yielding $\beta_0 > 0$, which has implications for the physical consequences of QCD. From Equation (1.8) it is obvious that for $\beta_0 > 0$ the value of α_s converges asymptotically to zero for high Q^2. This is the fundamental phenomenon of QCD, called *asymptotic freedom* mentioned above. It describes the behavior of quarks, which interact strongly at large distances (or small transverse momenta) and weakly at small distances (or large transverse momenta). Under these conditions the QCD interactions are thought to be weak at high temperatures and densities, which can be achieved in heavy-ion collisions. Therefore, a new phase of matter called quark-gluon plasma may occur.

On the other hand, we can choose a convenient momentum scale $\Lambda_{\mathrm{QCD}} = \mu e^{-2\pi/(\beta_0 \alpha_s(\mu^2))}$, which allows us to rewrite Equation (1.8) as:

$$\alpha_s(Q^2) = \frac{4\pi}{\beta_0 \log(Q^2/\Lambda^2)}. \tag{1.10}$$

This equation implies that there is a momentum scale $\Lambda_{\mathrm{QCD}} \approx 200$ MeV at which α_s diverges in the first order. Near this scale the perturbative expansions of QCD cannot be performed and the Feynman diagram approach becomes problematic[1] (as opposed to the region of high momenta). This region of small transferred momenta is governed by the second important phenomenon of QCD called *color confinement*. This phenomenon explains the fact that no color charged particles (such as quarks or gluons) can ever be isolated and directly observed in our laboratories, because they are confined by the strong interaction. We can only observe particles carrying zero net color charge (e.g., baryons and mesons) [7]. The strong force favors confinement because at a certain range it is more energetically favorable to create a quark-antiquark pair than to continue to increase the distance between the quarks.

Figure 1.2 summarizes the Q^2 dependence of α_s from various experiments and calculations.

1.2   The QCD Phase Diagram

Phase diagrams are often used when physicists want to summarize the properties of matter over a range of various physical quantities. The control parameters in this case are temperature T and baryon chemical potential μ_B. The chemical potential can be intuitively thought of as a measure of net baryon density of the system [9]. In general, chemical potential describes the change of internal energy due to the change of the composition of the system (in our case, the number of baryons).

The phase diagram of quark matter is not very well known, both experimentally and theoretically. Figure 1.3 shows the contemporary view of the QCD

---

[1]The calculations in this regime come from lattice QCD, in which the the action of the QCD Lagrangian is numerically calculated on a grid or lattice of points in space and time.
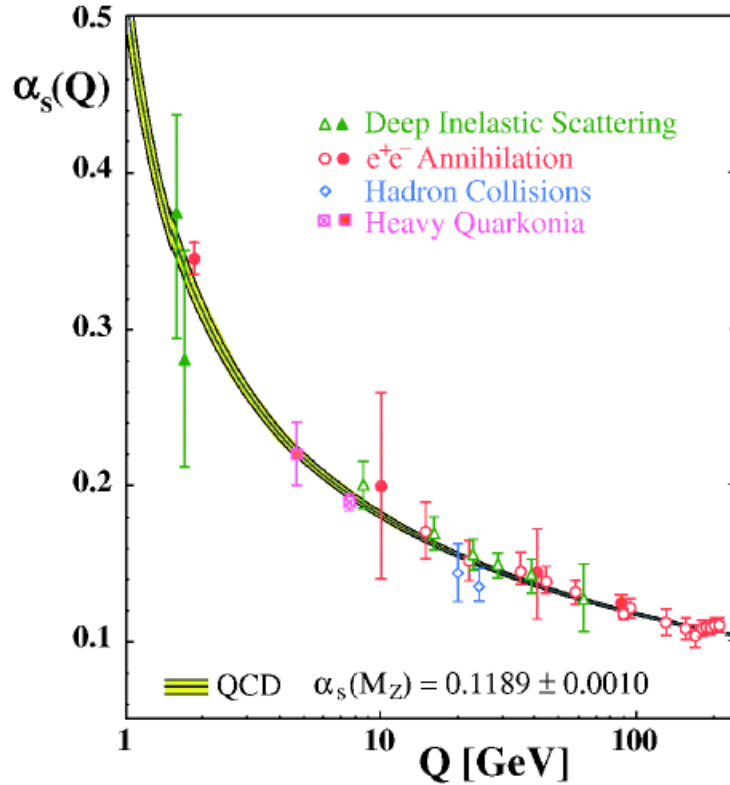
Figure 1.2: Summary of measurements of $\alpha_s(Q^2)$ as a function of the respective momentum scale Q, from [8].

phase diagram. It is a compilation of a body of results from model calculations, empirical nuclear physics, as well as first principle lattice QCD calculations and perturbative calculations in asymptotic regimes. Each point on the diagram represents the state of thermodynamic equilibrium, characterized by the coordinates in $T \times \mu_B$ space. Phase coexistence lines are illustrated as solid blue lines, crossover region by dashed line. Filled circles represent critical points.

Let us now begin at the point in the vacuum where $T = \mu_B = 0$. As we move along the horizontal axis the temperature and the density are zero up to the point of $\mu_B \approx 920$ MeV where the density jumps to nuclear density. The process of crossing the coexistence lines is believed to be the *first-order phase transition*. This process exhibits a discontinuity in the first derivative of the free energy with respect to pressure and temperature. Looking at the Figure 1.3 we see that there is yet another coexistence line between the hadron gas (lower T), and quark-gluon plasma (higher T). This first-order transition line is now ending at a point known as the QCD critical point. Beyond this point it is believed that the first-order phase transition between a hadron gas and QGP changes to a smooth cross over. This is the area explored by ultrarelativistic heavy-ion colliders [11].

A critical point is a well-defined singularity on a phase diagram, and is an attractive theoretical and experimental target to determine. Many theoretical calculations have been done and their predictions vary widely (ten of these results are summarized in [10]). Even though the exact location of the criti-
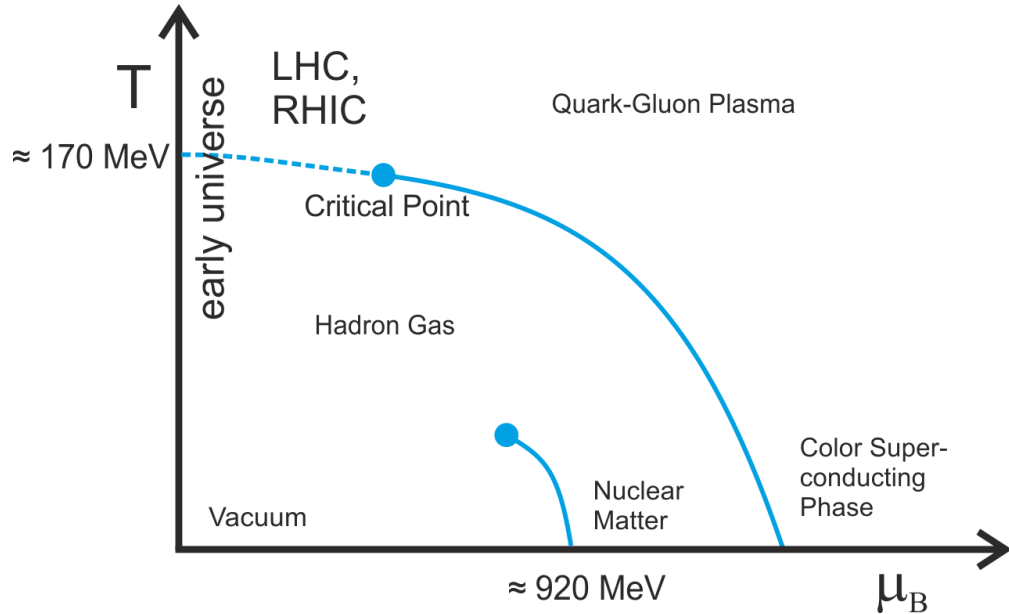
Figure 1.3: Schematic semi-quantitative sketch of the QCD phase diagram showing the names of the various phases. For guidance , aslo shown are the typical values of μ_B and T in heavy-ion collision experiments (LHC, RHIC) and in the early universe. Based on [10].

cal point is not known yet, the available theoretical estimates suggest that the point is within the region of the phase diagram probed by the heavy-ion collision experiments. This raises the possibility to discover this point in such experiments [12].

In addition to the discussed transitions and phases, other abnormal forms of nuclear matter can exist at high densities. Exotic states such as quark liquids and color superconductors (systems with locked color) are thought to exist [13].

1.3 Heavy Ion Collisions

The QGP can exist only in extreme conditions of very high energy densities and temperatures. In order to recreate matter at these conditions in the terrestrial laboratory, one collides heavy nuclei (heavy ions) at ultrarelativistic energies[2]. Previous attempts to study the properties of the QGP created in heavy-ion collisions have been made at the Brookhaven National Laboratory on Long Island (NY, USA) at the Relativistic Heavy Ion Collider (RHIC), which was the world's highest energy accelerator of heavy ions before the launch of the Large Hadron Collider (LHC) in 2008 [14]. Further details about the LHC machine will be discussed in Chapter 3.

In center-of-mass frame, as they fly towards each other, the colliding nuclei appear as two Lorenz-contracted discs. It is expected that during the collision,

---

[2]The energy region of ultrarelativistic heavy ion reactions starts at around $10\ \mathrm{GeV}$ center-of-mass energy.

the nuclei deposit a large amount of energy into a very small volume in the collision region. As estimated by Bjorken [15], the energy density can be so high that these reactions might provide the conditions for the creation of the QGP.

The most frequent events in low energy nuclear physics ($\sqrt{s_{\mathrm{NN}}} \approx 1$ MeV) are elastic collisions and low energy inelastic collisions. In both cases the final multiplicity (the number of particles after the reaction) is quite small. However, the multiplicities in (ultra)relativistic heavy-ion collisions are very large. The number of produced particles may exceed one thousand, which is much more than the number of initial nucleons [16]. This leads to special experimental requirements. For example the track recognition problem becomes very difficult at large multiplicities leading to a need of an effective tracking detector. It is also advantageous if we can detect all of the created particles in an event. Because of this, it is desired for the detector to cover full 2π in azimuth. As we will see, these conditions are partially fulfilled by the ATLAS detector at LHC (see Section 3.2).

1.4   The Glauber Model and Concept of Centrality

Since the colliding nuclei are extended objects with non-zero volume, the size of the interacting region depends on the impact parameter b of the collision. This physical quantity is defined as the distance between the centers of the colliding nuclei in a transverse plane (see Figure 1.4). Because it is impossible to directly measure the value of b [17], physicists introduced the concept of the centrality of the collision, which is directly related to the impact parameter of the collision.
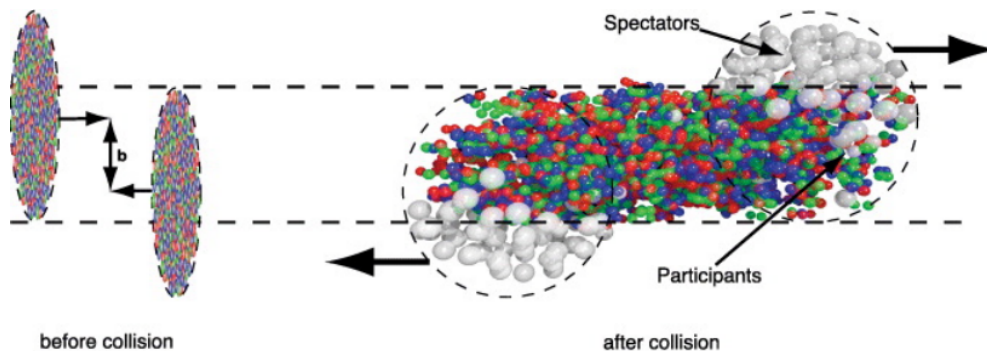
Figure 1.4: Left: the two heavy ions before the collision with the impact parameter b. Right: the spectators remain unaffected while in the participant zone, particle production takes place. Figure adapted from [18].

The geometrical Glauber model of multiple collisions [19–21] treats a nuclear collision as a superposition of binary nucleon-nucleon interactions. The density distribution of nucleons in a nucleus is typically parametrized by two-

parameter Woods-Saxon distribution given by:

$$\rho(r) = \rho_0 \frac{1}{1 + \exp\left(\frac{r-a}{R}\right)},$$ (1.11)

where a represents the "surface thickness" of the nucleus and $R = r_0 A^{1/3}$ is the nuclear radius parametrized with mass number A and experimentally determined constant $r_0 = 1.25$ fm. The constant ρ_0 ensures proper normalization.

The variables used to quantify the collision centrality in this model include the number of participant nucleons N_{part} (that is the number of nucleons that undergo at least one collision) and the number of all nucleon-nucleon collisions N_{coll}. Assuming that nucleons follow independent straight trajectories through the colliding system we can calculate these quantities for a given value of the impact parameter.

One of the techniques used to determine the values of N_{part} and N_{coll} is Monte Carlo. In this case the distribution (1.11) is used to populate two nuclei. Then, a random impact parameter is generated, thus defining an offset between the nuclear centers. Finally, the transverse projection of one of the nuclei on another is done and for every nucleon from the first nucleus the transverse distance to every nucleon in the second nucleus is determined. If this distance is less than $\sqrt{\sigma_{\mathrm{inel}}^{\mathrm{NN}}/\pi}$ (where $\sigma_{\mathrm{inel}}^{\mathrm{NN}}$ is the total inelastic cross-section of two nucleons), the nucleons are said to have participated and N_{coll} is incremented. The number of nucleons for which this condition is satisfied at least once is then N_{part}.

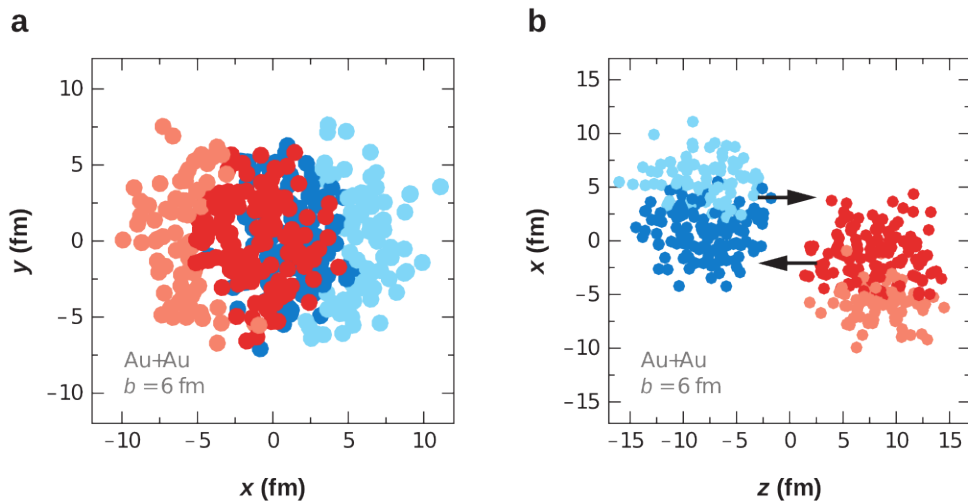An illustration of such a Glauber Monte Carlo (GMC) event for an AuAu collision is shown in Figure 1.5.

Figure 1.5: An AuAu GMC event with impact parameter $b = 6$ fm viewed (a) in the transverse plane and (b) along the beam axis. Darker circles represent participating nucleons. Ref. [21].

While these geometrical quantities are, together with the impact parameter, unobservable, previous studies at RHIC and SPS have shown that the multiplic-

ity and total transverse energy E_T are strongly correlated with N_part. Multiplicity or total E_T are, therefore, used to quantify the centrality in an experiment.

A measure of centrality used at the ATLAS experiment at LHC is a total transversal energy deposited in forward calorimeters FCal. Once the total E_T is summed up, the data sample is sorted in this variable, and split into fractions of equal cross-section, which are commonly called *centrality bins*. The convention is to quote the fractional value in terms of percentage, e.g. $0-10\%$, $10-20\%$, $\ldots\ 90-100\%$. Using the GMC procedure described above, the mean and the spread (RMS) values of the b, N_part, and N_coll for five selected centrality bins together with their respective systematic uncertainties can be extracted and are listed in Table 1.1. The main thing to remember is that smaller percentages correspond to more central events. More detailed description of this concept and the method of centrality determination used at ATLAS is given in Section 4.1.3.

Centrality	b mean [fm]	b RMS [fm]	N_part mean	N_part RMS	N_coll mean	N_coll RMS
$0-10\%$	3.4 ± 0.1	1.2	355 ± 3	33	1484 ± 120	241
$10-20\%$	6.0 ± 0.2	0.8	261 ± 4	30	927 ± 82	183
$20-30\%$	7.8 ± 0.2	0.6	187 ± 5	23	562 ± 53	124
$30-50\%$	9.9 ± 0.3	0.8	108 ± 5	27	251 ± 28	101
$50-100\%$	13.6 ± 0.4	1.6	22 ± 2	19	30 ± 5	35

Table 1.1: Values of parameters extracted from the Glauber Monte Carlo. Ref. [22, 23].

1.5   Jets in QCD

Let us first consider a collision of simple "QCD systems", for example two protons[3]. During a large-momentum-transfer scattering processes in high-energy collisions, as the original quarks inside the protons separate, the energy of the strong nuclear field between them increases up to the point when there is enough energy to create a new quark-antiquark pairs [24]. Due to postulated confinement, the quarks escaping from the collision cannot exist individually. Instead, free quarks created in collision combine with quarks and antiquarks created spontaneously from the vacuum to form hadrons [25]. This process is called *hadronization* and leaves us with two sets of hadrons traveling in the opposite directions. They are usually collimated in two cones around the direction of the two original partons and we refer to them as *jets*. However, this concept of jet, which is associated with the shower of an originating hard parton that has undergone hadronization, must be made more specific in order to be used as an experimental or theoretical concept. Schematic picture of the jet production in proton-proton (pp) and lead-lead (PbPb) collision is shown in Figure 1.6.

---

[3]We call these systems simple because, as opposed to the much more complex systems encountered in heavy-ion collisions, only few of the partons interact.
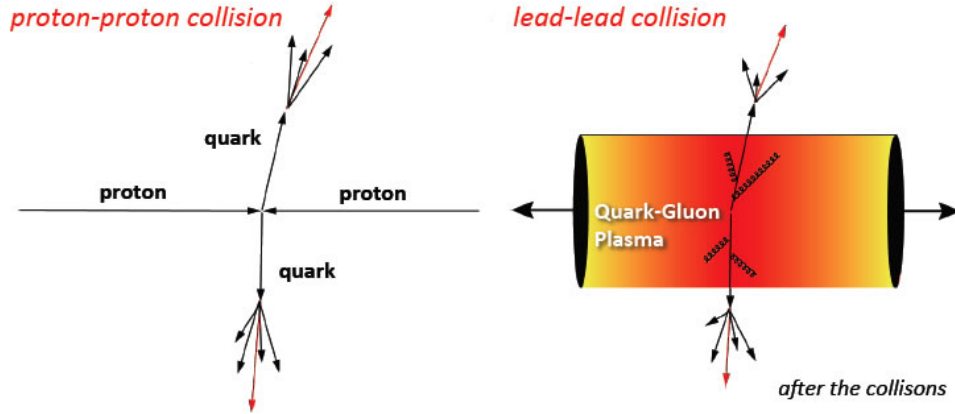
Figure 1.6: Sketch of a hard scattering, showing the jet production in proton-proton (left) and lead-lead (right) collisions. The colliding nuclei in the right picture are displayed as thin discs due to the Lorenz contraction. Note that the jets created in heavy-ion collision are modified due to the interactions of quarks with the QGP. Ref. [26].

The QCD theory related to jets is very broad containing e.g. the higher order QCD calculation, parton showers, fragmentation and hadronization. These topics are beyond the scope of this thesis and we will not discuss them. Instead, in the remainder of this section, we will concentrate on the jet algorithms.

Since we cannot measure the original parton, jet has to be defined by a jet finding algorithm. *Jet reconstruction* is a procedure by which the momenta of the jet fragments are resummed back to obtain the momentum of the original parton, basically undoing the process of fragmentation. In other words, it is a set of rules that postulate how to cluster the products of the hadronization and fragmentation into an object whose kinematics is as close as possible to the kinematics of the original parton.

In simple systems, such as electron-positron annihilations into two or three final state partons the definition of jets is simple and to a large extent unambiguous. Unfortunately, the situation turns out to be much more complicated if more partons in the final state are taken into account and other processes, such as hadron-hadron collisions, are analyzed.

An ideal jet finding algorithm would include all of the hadrons that come from the fragmentation of the original parton and exclude those coming from a different parton or other processes. Unfortunately, QCD does not allow us to unambiguously separate the final state hadrons into those originating from the original hard-scattered parton and those that do not (e.g. those coming from the interactions of other initial partons). As a consequence, a jet is not uniquely defined and different jet algorithms may produce different resulting jets.

There are two main types of jet algorithms: a cone algorithm and a sequential (or clustering) algorithm. Sequential recombination algorithms work by iteratively combining pairs of particles (defined by their four-momenta p^μ) in a specified way until the procedure terminates and returns the set of jets. So in

order to characterize a sequential algorithm we need to specify following conditions: the method for deciding which particles to combine, the scheme to be used to combine the momenta of the particle pair and the criterion for stopping the iteration.

We shall now outline basic steps of the k_t algorithm, which belong to the family of sequential jet algorithms and was first proposed to be used in electron-positron collisions [27] and later adapted for hadronic collisions [28]. This algorithm uses a specific distance d_{ij} between particles i and j and a distance between particle i and the beam axis, d_{iB}, to construct the recombination rule. These quantities are defined as

$$d_{ij} = \min(p_{\mathrm{T}i}^2, p_{\mathrm{T}j}^2)\frac{\Delta R_{ij}^2}{R^2}, \qquad d_{iB} = p_{\mathrm{T}i}^2, \tag{1.12}$$

where

$$\Delta R_{ij} = \sqrt{(\eta_i - \eta_j)^2 + (\phi_i - \phi_j)^2} \tag{1.13}$$

is a distace in $\eta \times \phi$ space. Here η and ϕ are the rapidity and azimuthal angle of a particle with p_{T} transverse momentum[4]. The algorithm starts with a list of *protojets*[5] with four-momenta p_i^μ and works as follows:

1. Calculate d_{ij} for all protojet pairs and d_{iB} for all protojets.

2. Find the minimum of d_{ij} and d_{iB}.

3. If the minimum is a d_{ij} combine these two protojets i and j into one, typically by simple four-momentum addition, and insert it back into the list.

4. If the minimum is a d_{iB}, remove this protojet from the list and call it a final-state jet.

5. Repeat this process until no protojets remain.

Since every iteration decreases the number of protojets in a list by one, the procedure terminates after number of iterations equal to the number of protojets in the initial list. The only free parameter of k_t algorithm is the distance parameter R, which controls the size of the jet. Default configurations in ATLAS are $R = 0.4$ for narrow and $R = 0.6$ for wide jets [29].

As we can deduce from Equation (1.12), due to a presence of the minimum function in d_{ij} definitions the algorithm clusters low-p_{T} (soft) particles first, thus going "backwards" in the fragmentation chain. That means the k_t algorithm allows jets clustered from the soft background particles to compete with the real jets. This feature presents a serious drawback of the classical k_t algorithm

---

[4]More detailed description of the kinematic variables used in high-enery physics and their properties is in Section 3.2.1.

[5]The elements of the initial list are commonly called "protojets" before the algorithm terminates and "jets" after. The protojet can be a particle, track, or a calorimeter tower.

both in proton-proton and heavy-ion collisions because, as opposed to e^+e^- collisions where the background is minimal, the hadronic collisions produce a very strong background interfering with the jets. In order to fix this problem, the distance measure of the k_t algorithm has to be generalized in the following way:

$$d_{ij} = \min(p_{\text{Ti}}^{2p}, p_{\text{Tj}}^{2p}) \frac{\Delta R_{ij}^2}{R^2}, \qquad d_{iB} = p_{\text{Ti}}^{2p}. \qquad (1.14)$$

It is obvious that for $p = 1$ we get the traditional k_t algorithm described above. The choice $p = 0$ corresponds to the Cambridge-Aachen algorithm [30] where the distance variable is angle and jets are clustered purely on a geometric basis. Finally, $p = -1$ defines the anti-k_t jet clustering algorithm [31]. The main virtue of this algorithm is that it first recombines high-p_T (hard) particles, effectively reducing the sensitivity of the algorithm to the internal structure of the parton shower. Moreover, the nature of this algorithm gives the anti-k_t jets their distinct and desired cone-like shape. For these reasons, both ATLAS and CMS have chosen the anti-k_t algorithm as the default jet algorithm for use in physics analysis.

1.6   Jet Quenching

One of the main differences between proton-proton collisions and heavy-ion collisions is the presence of the QGP in the latter. In these conditions the products of the potential scattering processes interact heavily with the ambient plasma. A rough classification of the types of energy-loss may be factorized into following two components [32, 33]:

- Energy is transmitted to nearby medium constituents via elastic processes, referred to as the collisional energy loss. This mode is believed to dominate at low-particle momentum or for initial partons with large rest mass.

- Medium-induced radiation of partons out of the cone due to the gluon bremsstrahlung ("gluonstrahlung") during the interaction with the medium, called radiative energy loss.

Feynman diagrams for both modes are sketched in figure 1.7.

It is expected that the radiative energy loss dominates over collisional energy loss. The amount of energy loss is predicted to be proportional to the energy density of the medium. Hence jets, which have lost significant amount of energy while propagating through the medium, can be used as probes of the medium, providing information about its structure and properties [33]. In this way jets play a distinct role in ultrarelativistic heavy-ion physics.

Bjorken was the first one who recognized the potential of jets as a tool to study the QGP. He suggested that high energy quarks and gluons suffer differential energy loss while propagating through the plasma [15]. He also pointed out the extreme case when the hard collision occurs at the periphery of the hot
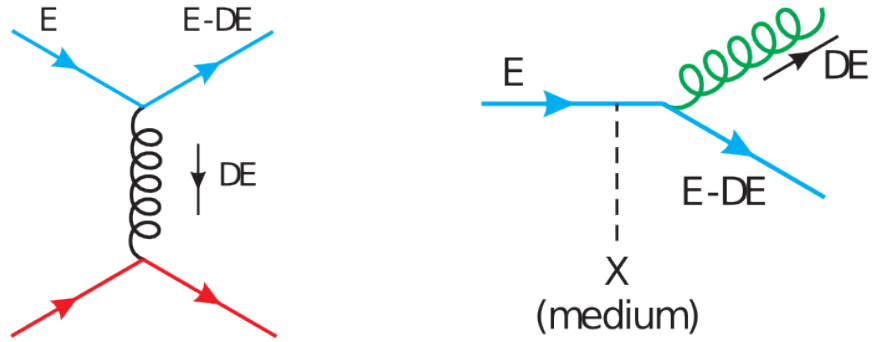
Figure 1.7: Diagrams for collisional (left) and radiative (right) energy losses of a quark of energy E traversing a quark-gluon medium. Ref. [34].

medium resulting in one jet being almost unquenched, and the other jet being totally absorbed. An example of such an event with large dijet asymmetry measured by the ATLAS experiment [35] is illustrated in Figure 1.8. In this figure one can see that one jet from a dijet system is fully quenched while the other seems to be unmodified. In the left panel a view along the beam axis is pictured with high-p_T charged particle tracks indicated by the lines and energy responses in calorimeters by colored bars. The middle panel shows the E_T distribution in $\eta \times \phi$ space. In the right paned a similar distribution is shown for the charged particle tracks in the Inner Detector. The signal in the Inner Detector is consistent with the calorimeter signal[6].

Jet quenching, or high-p_T parton suppression, has already been observed in the collisions of golden nuclei at RHIC [36], but the LHC heavy-ion program allows to study this phenomenon at much higher energies than previously achieved at RHIC and, therefore, to use fully reconstructed jets [35].
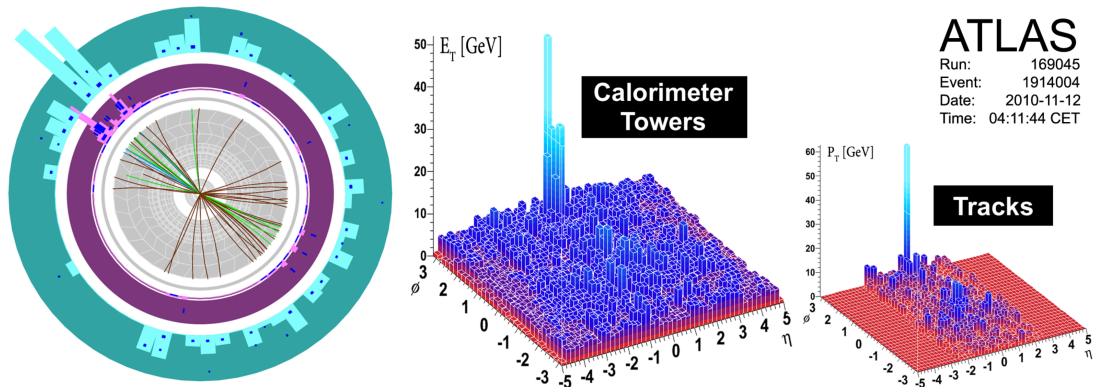

Figure 1.8: Event display of a highly asymmetric dijet event, recorded by ATLAS during the early portion of the 2010 PbPb run, with one highly energetic jet and no visible recoiling jet. Ref. [35].

---

[6]Mentioned physical quantities and experimental apparatus are further discussed in section 3.2

Chapter 2

Motivation and Previous Measurements

At this point it is instructive to outline a brief motivation and goals of the analysis presented in this thesis. The first direct observation (that is using high statistics sample of fully reconstructed jets) of jet quenching was performed at the ATLAS detector at the LHC in year 2010. These results were published in article [35]. This study focused on the balance between the highest energy pair of jets in events where the azimuthal separation of these two jets was more than $\pi/2$. The jet energy imbalance was expressed in terms of the asymmetry A_{J} defined as:

$$A_J = \frac{E_{\mathrm{T1}} - E_{\mathrm{T2}}}{E_{\mathrm{T1}} + E_{\mathrm{T2}}}, \tag{2.1}$$

The dijet asymmetry distributions are shown in four centrality bins in top row of Figure 2.1 where they are compared with Monte Carlo simulated events and proton-proton data. As we can see the asymmetry distribution in peripheral (leftmost panel) lead-lead events coincides with the one for proton-proton and simulated data. As we move towards more central collisions, however, one can observe that lead-lead data develop different characteristics. Especially for the most central $(0-10\%)$ lead-lead events the A_{J} distribution broadens and the mean shifts to higher values. The panels in bottom row show that the leading and subleading jets are still ejected primarily in back-to-back configuration.

This has, of course, a natural interpretation in terms of QCD energy loss caused by the propagation through a hot, dense medium created primarily in central lead-lead collisions. Namely that the subleading jet is often strongly "quenched" leading to the observed imbalance in the jet energy of the two jets in the dijet system.

The main goal of the analysis presented in the following chapters is to provide information about the mechanism that is responsible for the loss of energy of the subleading jets compared to the leading jet in unbalanced dijet events. To accomplish this, the differences in the redistribution of "lost" energy are studied as a function of the associated charged particle transverse momentum. The distributions are extracted for several PbPb centrality bins, and are furthermore
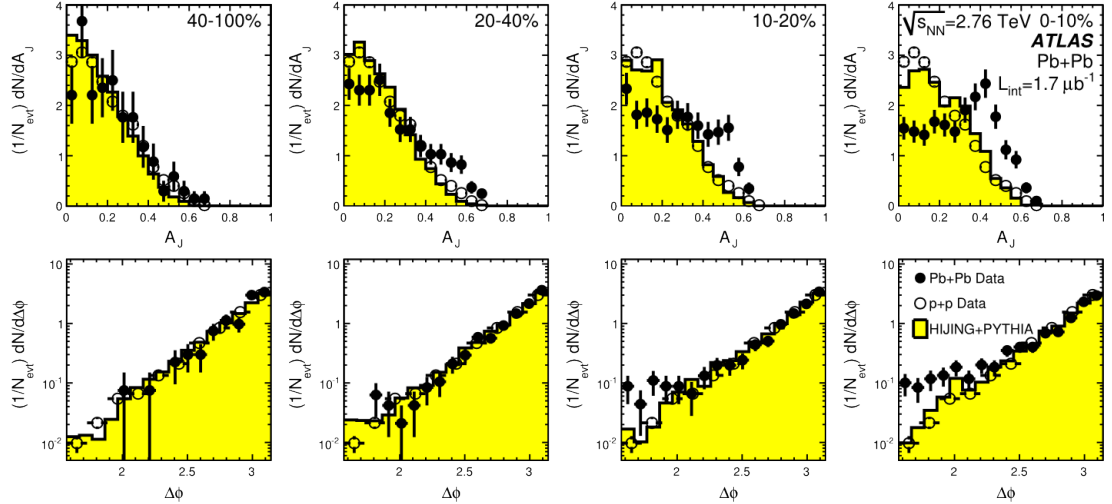
Figure 2.1: (Top) Dijet asymmetry distributions for data (points) and unquenched HIJING with superimposed PYTHIA dijets (solid yellow histograms), as a function of collision centrality (left to right from peripheral to central events). Proton-proton data froms $\sqrt{s} = 7$ TeV, analyzed with the same jet selection, are shown as open circles. (Bottom) Distribution of the azimuthal angle between the two jets, for data and HIJING + PYTHIA, also as a function of centrality. Taken from Ref. [35].

studied as function of dijet asymmetry.

In order to gain more insight into the flow of the "quenched" energy, one can study the overall momentum balance of dijet events. This can be done using so-called missing transverse momentum[1] (missing p_T), which is basically the sum of transverse momenta of all particles in the studied track p_T range with a minus sign[2]. By studying the projection of the missing p_T on the axis of the leading jet as a function of dijet asymmetry, it is possible to inspect the redistribution of the "lost" energy by the leading and subleading jets. This analysis has been previously done by the CMS Collaboration at the LHC and was first published in [22] in 2011 and with updated results in 2014 [37]. The final figures taken from these publications are shown below in Figures 2.2 and 2.3. An interpretation of the results by CMS will be provided in the context of our analysis in Chapter 5.

---

[1] If the sign for the vectorial quantity is not in boldface it denotes the magnitude of the vector.

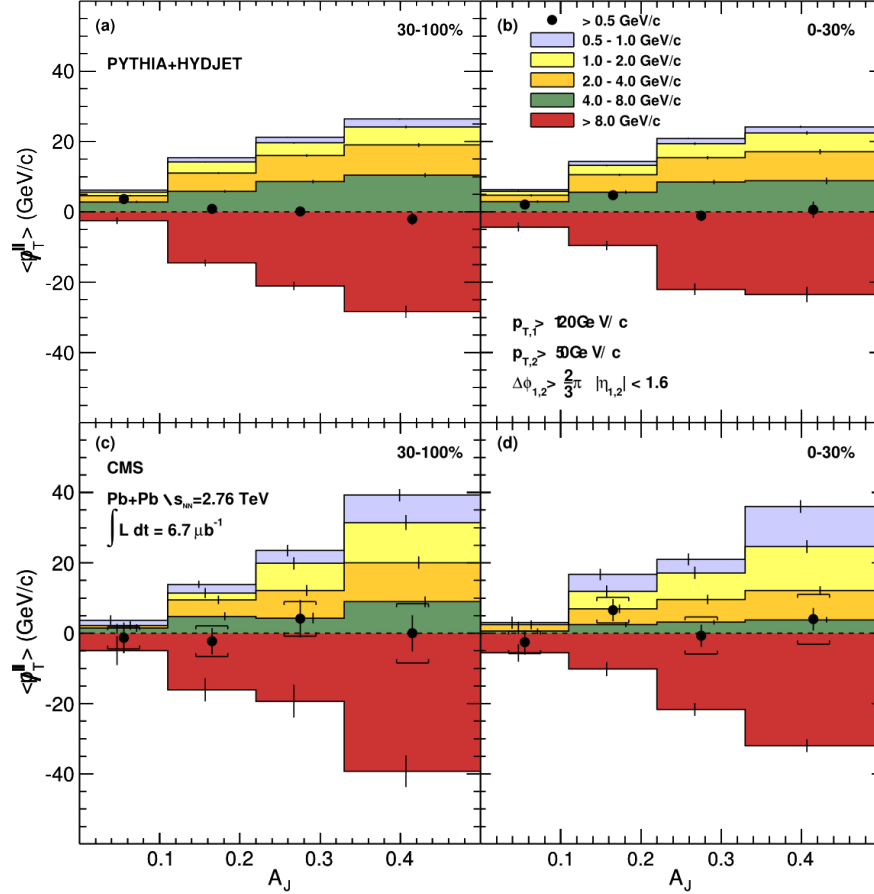[2] A more detailed definition of this quantity is given in Section 4.2.

Figure 2.2: Average missing transverse momentum, $\langle \displaystyle{\not}p_{\mathrm{T}}^{\parallel,\mathrm{LJ}} \rangle$, for tracks with $p_{\mathrm{T}} > 0.5$ GeV/c, projected onto the leading jet axis (solid circles). The $\langle \displaystyle{\not}p_{\mathrm{T}}^{\parallel,\mathrm{LJ}} \rangle$ values are shown as a function of dijet asymmetry A_{J} for $30 - 100\%$ centrality (left) and $0-30\%$ centrality (right). For the solid circles, vertical bars and brackets represent the statistical and systematic uncertainties, respectively. Colored bands show the contribution to $\langle \displaystyle{\not}p_{\mathrm{T}}^{\parallel,\mathrm{LJ}} \rangle$ for five ranges of track p_{T} . The top and bottom rows show results for PYTHIA + HYDJET and PbPb data, respectively. For the individual p_{T} ranges, the statistical uncertainties are shown as vertical bars. Taken from Ref. [22]
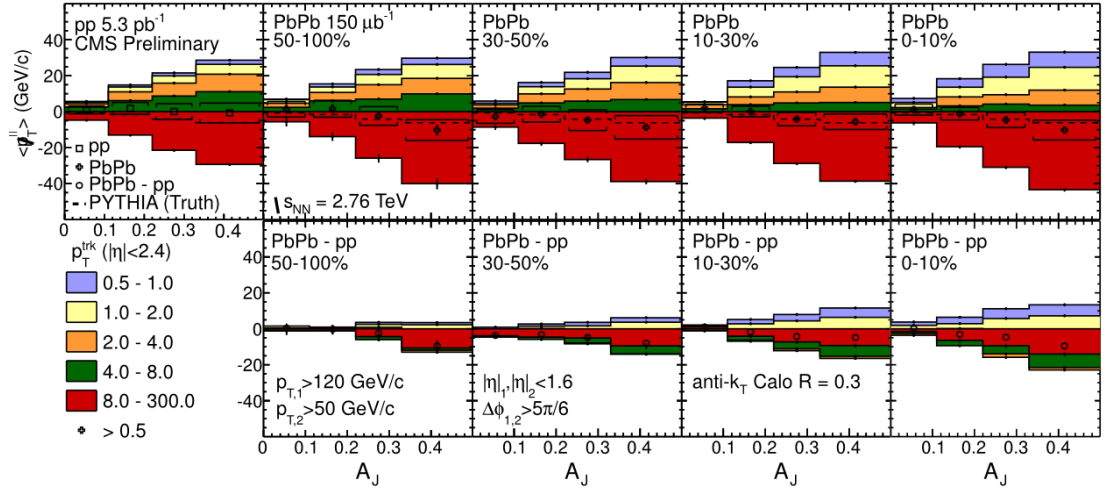
Figure 2.3: (Upper row) Average missing transverse momentum, $\langle \not{p}_T^{||,\mathrm{LJ}} \rangle$, for pp collisions (left) and four selections of PbPb collision centrality ranging from $50 - 100\%$ to $0 - 10\%$. The solid markers show $\langle \not{p}_T^{||,\mathrm{LJ}} \rangle$ averaged over all tracks with $p_T > 0.5$ GeV/c, while the colored boxes show the contribution to $\langle \not{p}_T^{||,\mathrm{LJ}} \rangle$ for various momentum ranges from $0.5 < p_T < 1$ GeV/c (light blue) to $p_T > 8$ GeV/c (red). For the solid circles, vertical bars and brackets represent the statistical and systematic uncertainties, respectively. For the individual p_T ranges, the statistical uncertainties are shown as vertical bars. (Lower row) Difference PbPb - pp of the $\langle \not{p}_T^{||,\mathrm{LJ}} \rangle$ contribution for the individual momentum ranges shown in the upper panel. Error bars and brackets represent statistical and systematic uncertainties respectively. Taken from Ref. [37].

Chapter 3

Experimental Setup

3.1 The Large Hadron Collider

The Large Hadron Collider (LHC) is a particle accelerator and collider located at CERN outside Geneva, Switzerland. It was primarily constructed to collide protons, however, the machine is also capable of colliding heavy ions. The first lead ion collisions took place in November 2010.

The LHC machine[1] is installed in the tunnel which was originally constructed for LEP (Large Electron–Positron Collider). The tunnel itself has 26.7 km in diameter and contains eight arcs and eight straight sections. It lies between 45 m and 170 m under the ground on the borders of Switzerland and France. By contrast to the particle-antiparticle colliders, the LHC accelerator is designed to collide particles with the same charge sign. For this reason it has two parallel rings with counter-rotating beams. Figure 3.1 shows the location of the LHC tunnel, and the location of the four large experiments around its ring.

As previously mentioned, the main physics program of LHC is based on proton-proton (pp) collisions. However, typically one month per year, runs with heavy-ion (^{208}Pb^{82+}) collisions are included. The LHC injector chain for Pb ions is almost identical to the one for protons. The ions go from source through a series of linear and circular accelerators before entering the LHC. The first of them is a linear accelerator Linac 3, after that the ions go through three circular accelerators, namely the Low Energy Ion Ring (LEIR), the Proton Synchrotron (PS) and the Super Proton Synchrotron (SPS). This sequence is also schematically shown in Figure 3.2.

The Pb^{27+} ions extracted from source need to be fully stripped from electrons before entering the LHC. This is assured by two aluminium foil strippers. The first one is located in Linac3 and provides the conversion to Pb^{54+}. The second stripping occurs in the line between PS and SPS. After extraction from PS the Pb beam is fully stripped by a 0.8 mm aluminium foil [40].

---

[1]If not stated otherwise, all information about the LHC were taken from the LHC design paper [38].
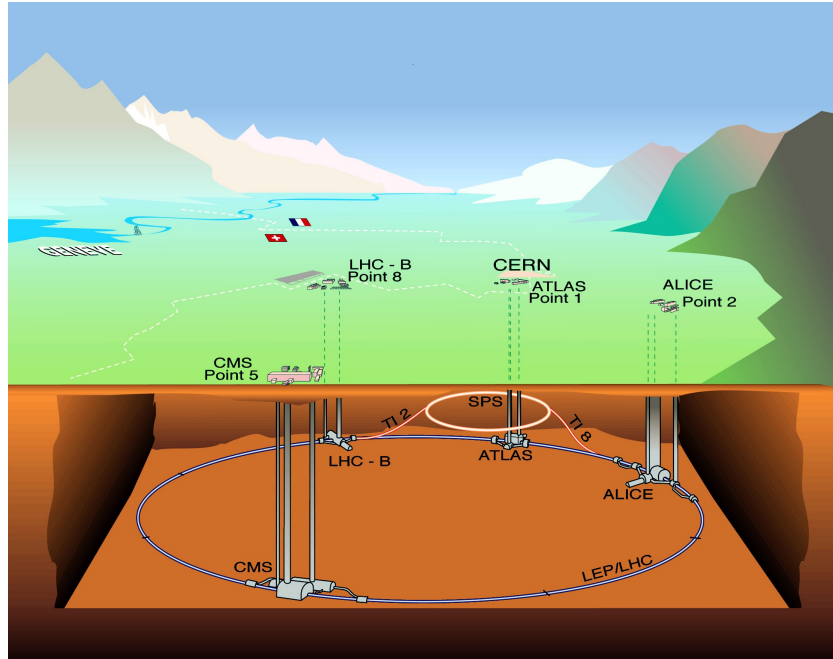
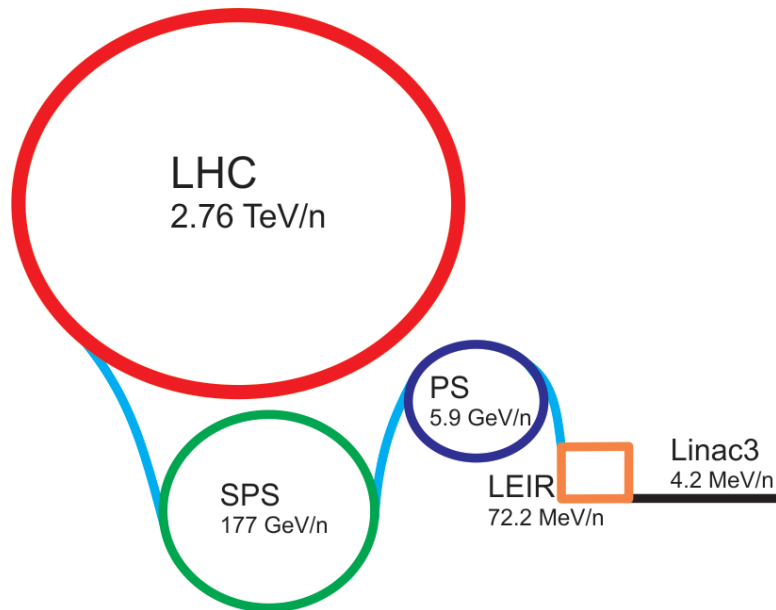Figure 3.1: Overall view of the LHC and its 4 main experiments. Ref. [39].

Figure 3.2: Scheme of the LHC ion injection chain with corresponding output energies per nucleus taken from [40].

3.2 The ATLAS Experiment

ATLAS[2] (A Toroidal LHC ApparatuS) is one of the seven particle detectors at the LHC and together with CMS (Compact Muon Solenoid) is one of two general purpose detectors. It is built at interaction point 1 (IP1) of the LHC ring and is capable of studying both pp and PbPb collisions at unprecedented luminosity. Its massive dimensions are 44 m in length, 25 m in height and it

---

[2]If not stated otherwise, all information about the ATLAS detector were taken from [41].

weighs about 7000 tons. The illustration on Figure 3.3 provides overall cutaway view of the ATLAS detector.

Following sections are devoted to the more detailed description of this detector. In Section 3.2.1 we will define several concepts and physical quantities which are often used in accelerator physics. This Section also defines the coordinate system used in the ATLAS experiment. The Section 3.2.2 then describes various parts and sub-detectors of ATLAS.
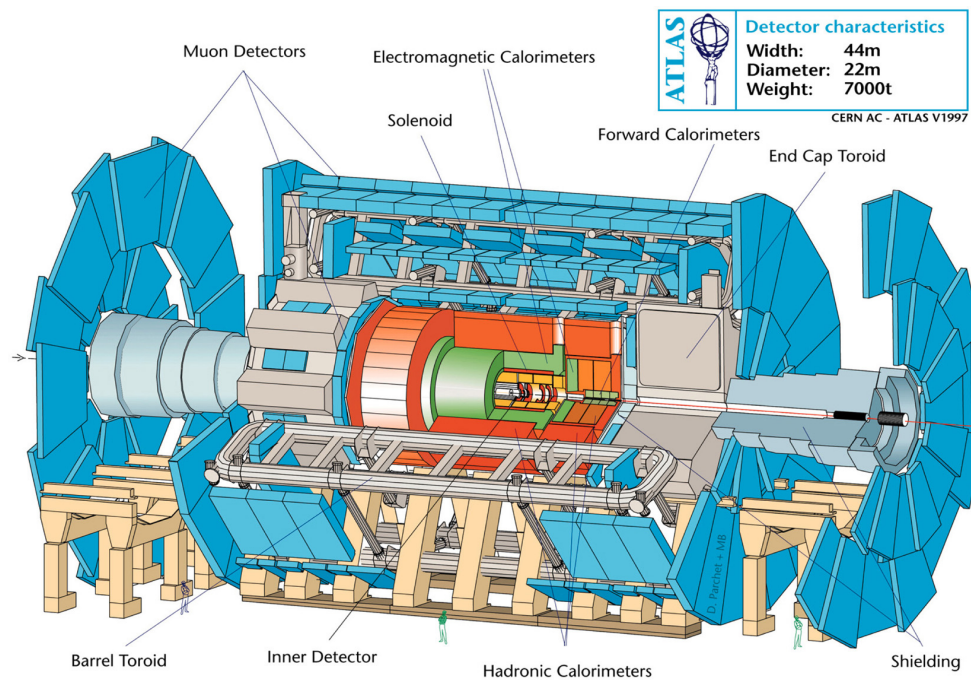

Figure 3.3: Cutaway view of the ATLAS detector highlighting various parts of the experiment [42].

3.2.1 The ATLAS coordinate system and related concepts

The origin of the ATLAS coordinate system is located in the nominal interaction point. The z-axis is defined by the beam direction while the x-y plane is perpendicular to the beam direction. The positive x-axis points towards the center of the LHC tunnel and the positive y-axis is defined as pointing upwards. The orientation of the z-axis therefore follows from the right-handedness of the coordinate system. The azimuthal angle ϕ is measured as the angle in the x-y plane. The $\phi = 0$ corresponds to the positive x-axis and increases clock-wise looking in the positive z direction. The polar angle ϑ is measured as the angle from the positive z-axis. By definition, ϑ is 0 or π along the beam axis and $\pi/2$ on the transverse plane.

Considering a particle with momentum vector $\mathbf{p} = (p_x, p_y, p_z)$ and energy E experimental particle physicists often use *rapidity* y as an alternative to speed

as a measure of motion. It is defined as [43]:

$$y = \frac{1}{2} \ln \left(\frac{E + p_z}{E - p_z} \right). \tag{3.1}$$

Rapidity is not Lorentz-invariant, it is, however, additive under the boosts along the z-axis. For $p \gg m$ or, equivalently, for $m/p \to 0$, the Equation (3.1) can be expanded and simplified to obtain the definition of *pseudorapidity*:

$$\eta = -\ln \left(\tan \left(\frac{\vartheta}{2} \right) \right). \tag{3.2}$$

This quantity gives us only geometric information about the direction of the particle and does not require the knowledge of mass of the particle. Unlike rapidity, pseudorapidity is not additive under longitudinal boosts.

We define the *transverse momentum* p_T as the projection of the momentum vector on the x-y plane:

$$p_T = |\mathbf{p}| \sin \vartheta = \sqrt{p_x^2 + p_y^2}. \tag{3.3}$$

The *transverse energy* E_T of a particle is defined as[3] [44]:

$$E_T = E \sin \vartheta = \sqrt{m^2 + p_T^2}, \tag{3.4}$$

where m is the rest (invariant) mass of the particle. Azimuthal angle ϕ, pseudorapidity η, E_T and p_T are four quantities that can fully characterize the particle. We can therefore say that E_T and p_T are measured in $\eta \times \phi$ space.

A total energy accessible in the collision is quantified by the *center-of-mass energy*, which can be expressed in the Lorentz invariant form[4] [43]:

$$\sqrt{s} = \sqrt{(P_1 + P_2)^2} = \sqrt{(E_1 + E_2)^2 - (\mathbf{p_1} + \mathbf{p_2})^2}, \tag{3.5}$$

where P_1 and P_2 are the four-momenta of the incoming particles.

In heavy-ion collisions, it is common to use the energy per nucleon-nucleon pair $\sqrt{s_{NN}}$. Typical values of $\sqrt{s_{NN}}$ for AuAu collisions at RHIC have been 130 GeV [45] and 200 GeV [36]. The LHC currently operates at 2.76 TeV per-nucleon center-of-mass energy and it is planned to reach $\sqrt{s_{NN}} = 5$ TeV, which roughly corresponds to designed 14 TeV for protons.

An important factor in a collider run is the *luminosity* which quantifies the yield of events per period of time normalized by the interaction cross-section. The beams in today's colliders consist of bunches of ions. If two bunches containing n_1 and n_2 particles collide head-on with frequency f, the *instantaneous*

---

[3]Using the convention where $c = 1$.

[4]This formula takes into consideration the collision of two particles with energies E_1 and E_2 and momenta vectors $\mathbf{p_1}$ and $\mathbf{p_2}$. The square of the momenta therefore plays the role of the dot product.

luminosity, $\mathscr{L}$, of a beam can be expressed as:

$$\mathscr{L} = f\frac{n_1 n_2}{4\pi\sigma_x\sigma_y}, \tag{3.6}$$

where σ_x and σ_y characterize the transverse beam profiles in the horizontal and vertical directions. It is assumed that the transverse profiles of the colliding bunches are identical and that the profiles are independent of position along the bunch. The integral over time of the instantaneous luminosity is the *integrated luminosity*. It is used to calculate the number of events N with cross section σ:

$$N = \sigma \int \mathscr{L}(t)\mathrm{d}t. \tag{3.7}$$

Luminosity is clasically stated in units of $\mathrm{cm^{-2}s^{-1}}$. Integrated luminosity, on the other hand, is usually quoted as the inverse of the standard measures of cross section, such as barns [43].

This thesis focuses on the phenomenon of jet quenching. It is therefore useful to define two more quantities regarding jets. One of them is the *jet axis* which characterizes the jet position in $\eta \times \phi$ phase space and gives the information about the direction of parton from which the jet originates. It can be defined e.g., as a transverse energy weighted position of constituents of jets:

$$\phi_{\mathrm{jet}} = \frac{\sum\limits_{i\in\mathrm{jet}} E_{\mathrm{T},i}\phi_i}{\sum\limits_{i\in\mathrm{jet}} E_{\mathrm{T},i}}, \qquad \eta_{\mathrm{jet}} = \frac{\sum\limits_{i\in\mathrm{jet}} E_{\mathrm{T},i}\eta_i}{\sum\limits_{i\in\mathrm{jet}} E_{\mathrm{T},i}}, \tag{3.8}$$

where η_i, ϕ_i and $E_{\mathrm{T},i}$ are the position in $\eta \times \phi$ space and transverse energy of constituents of jets. Constituents of jets are particles or calorimeter cells that are assigned to a jet by the jet finding algorithm mentioned in Section 1.5. Each jet finding algorithm has a distance parameter, or *radius*, R, which is the area in $\eta \times \phi$ space that is covered by a jet.

3.2.2 The sub-detectors

The ATLAS detector is forward-backward symmetric with respect to the interaction point and covers almost the full 2π in azimuth. It consists of four main subdetector systems [42].

- **The Inner Detector (ID):** This is the innermost sub-detector beginning only 50 millimeters from the beam axis. It has a cylindrical shape with a length of 7 m and the outer radius of 1.15 m. These dimensions cover a pseudorapidity region of $|\eta| < 2.5$. Its main purpose is the tracking of the charged particles and measuring their momentum. It is also capable of reconstructing the primary interaction vertex and particle decay vertices. Figure 3.4 contains the illustration of this sub-detector.
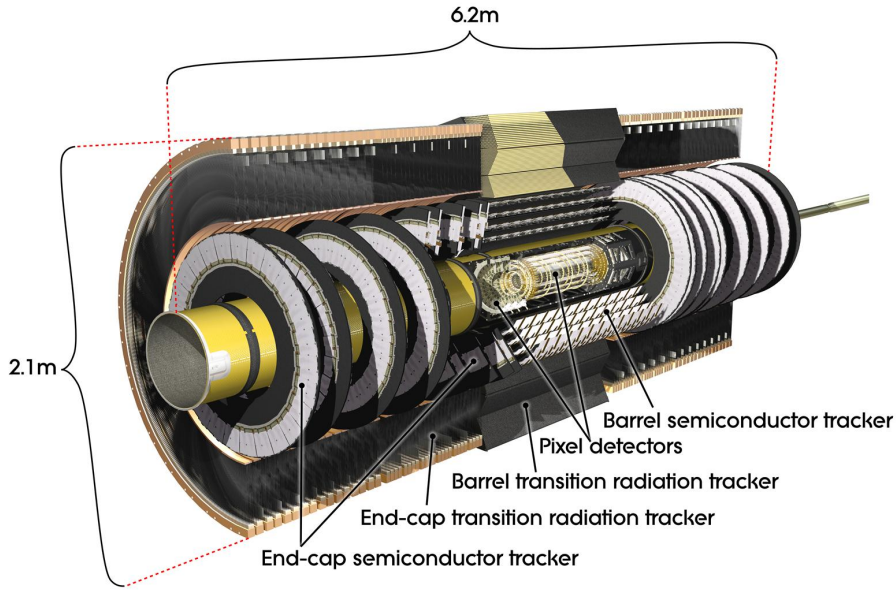
Figure 3.4: Overall view of the Inner Detector [42].

The ID is immersed in the solenoidal magnetic field of 2 T which curves the tracks of charged particles allowing the momentum measurements. The detector is composed of three independent sub-detectors. These are (in order of increasing radius): silicon pixel detector, a silicon microstrip detector (SCT) and, finally, a straw tube transition radiation tracker (TRT).

- **The Calorimeter System:** The ATLAS calorimeters are designed to stop the particles through the electromagnetic and strong interactions. This system is composed of electromagnetic (EM) and hadronic calorimeters, each using a different technology to measure the energy of particles. Liquid argon technology (LAr) is used by the EM calorimeters (and some hadronic calorimeters) and scintillation tiles by the hadronic ones. The fine segmentation of both types of calorimeters is well-suited for measuring jets [35].

When the particle strikes an absorber (thick metal layer) it initiates EM and/or hadronic showers. The energy of the incident particle is spread among the lower energy particles in the cascade. Behind the absorber is placed an active material which collects some of the energy of these particles, either through ionization (LAr) or scintillation (tiles). Alternating layers of absorber and active material are placed in succession and the shower-sampling is repeated. As a consequence, the energy of the particle can be determined.

In order to limit punch-through of the particles into the muon system the thickness of the calorimeters is an important parameter. Moreover, the absorbing material is chosen to be dense in order to absorb the particles. Figure 3.5 highlights various parts of the ATLAS calorimetric system. The EM calorimeter covers the pseudorapidity range of $|\eta| < 3.2$. The hadronic

27

calorimetry which uses the steel and scintillating tiles covers the range of $|\eta| < 1.7$. LAr technology is also used in hadronic end-cap calorimeters covering the range of $1.5 < |\eta| < 3.2$. Finally, the LAr forward calorimeters (FCal) extend the pseudorapidity coverage up to $|\eta| = 4.9$. As we will see in section 1.4 the FCal system plays a special role in the ATLAS heavy-ion analyses.
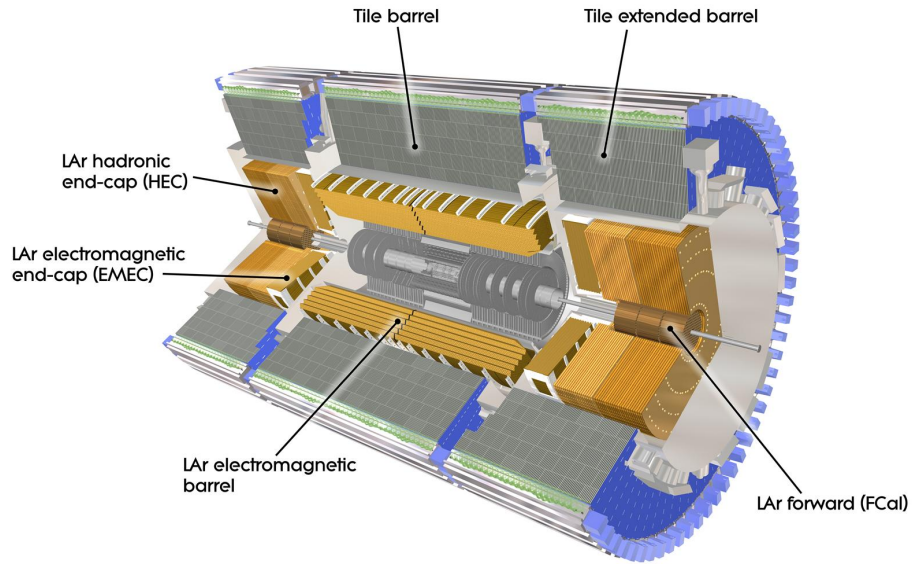
Figure 3.5: Cutaway view of the ATLAS calorimeters [42].

- **The Muon Spectrometer:** Figure 3.6 shows the layout of the muon spectrometer. This system is located on the outermost part of the detector
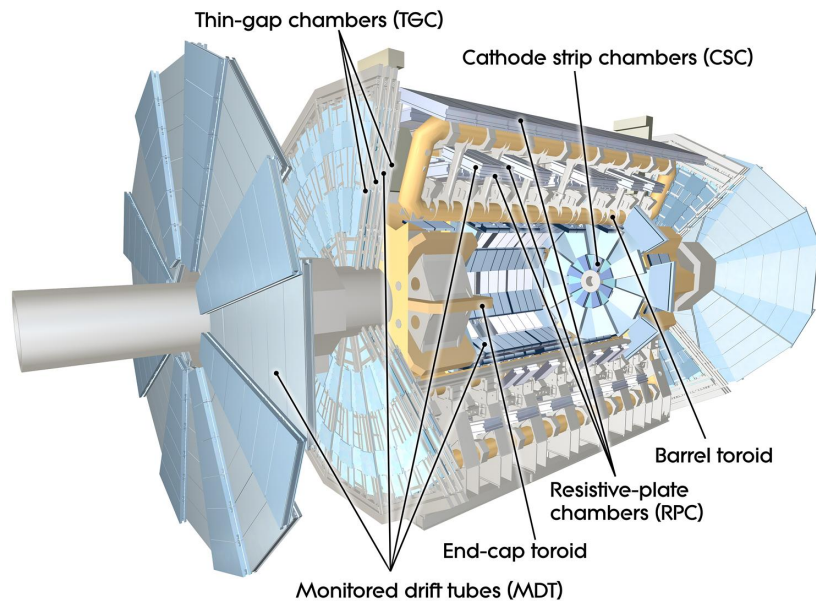
Figure 3.6: Layout of the muon spectrometer [42].

(see Figure 3.3) because the muons with sufficient energy are the only detectable particles that can pass the calorimetric system without being stopped. It consists of monitored drift tubes (MDTs) for precision tracking in the spectrometer, Resistive Plate Chambers (RPCs) and Thin Gap Chambers (TGCs) for triggering in barrel and endcap, respectively, and Cathode Strip Chambers (CSCs) for detailed measurements in the high-rate endcap inner layer where MDTs would have occupancy problems. Like in the ID the momenta of muons are measured using a magnetic field provided by the magnets described in the following paragraph.

- **The Magnet System:** The main purpose of this system is, as previously mentioned, bending the tracks of the charged particles for precise momentum measurements. It consists of the magnets used in the ID (central solenoid) and the muon spectrometer. The system of magnets for the latter consists of large barrel toroid for $|\eta| < 1.4$, two smaller end-cap magnets for the range $1.6 < |\eta| < 2.7$ and by the combination of the two in the transit region ($1.4 < |\eta| < 1.6$). The central solenoid produces an axial magnetic field throughout the ID.

Chapter 4

Basic Observables

4.1 Centrality Definition and Event Selection

4.1.1 Event selection

In this thesis, two sets of experimental data samples have been analyzed. The data were collected during the 2011 Heavy Ion run at $\sqrt{s_{\mathrm{NN}}} = 2.76$ TeV using jet trigger (Hard Probe stream) and minimum bias trigger (Minimum Bias stream).

- Minimum Bias PbPb collisions were identified using the Minimum-Bias Trigger Scintillator (MBTS) counters and Zero-Degree Calorimeters (ZDCs). The ZDCs are located symmetrically at $z = \pm 140$ m and cover $|\eta| < 8.3$. In PbPb collisions the ZDCs measure primarily "spectator" neutrons, which originate from the incident nuclei and do not interact hadronically. The MBTS counters are positioned 3.6 m from the nominal interaction point and provide the full coverage of the azimuthal angle ϕ in the region of pseudorapidity $2.09 < |\eta| < 3.84$. They are divided into eight ϕ and two η sectors, allowing for 16 possible hits per detector side [41, 46]. The total integrated luminosity corresponding to this data sample is approximately $0.7 \ \mu\mathrm{b}^{-1}$.

- The Hard Probe stream events with high-p_{T} jets were selected using a combination of a Level-1 minimum bias trigger and High Level Trigger (HLT) jet triggers. The Level-1 trigger required a total transverse energy measured in the calorimeter of greater than 10 GeV. The HLT jet trigger ran the offline PbPb jet reconstruction algorithm, described above, except for the application of the final hadronic energy scale correction, to identify jets with radius $R = 0.2$. The HLT trigger selected events containing a $R = 0.2$ jet with transverse energy $E_{\mathrm{T}} > 20$ GeV. The jet data sample corresponds to the total integrated luminosity of approximately $140 \ \mu\mathrm{b}^{-1}$.

In order to select a pure data sample of inelastic hadronic collisions, several offline selections had to be applied to the triggered event samples. Events selected by both minimum bias and HLT triggers were required to have a primary

vertex reconstructed from charged-particle tracks with $p_T^{ch} > 0.5$ GeV. The primary vertices were reconstructed from hits in the inner detector using the ATLAS track reconstruction algorithm described in [47] with settings optimized for high-multiplicity heavy ion collisions [48]. Additionally, the time difference between the two MBTS detectors is chosen to be less than 7 ns to efficiently reject beam-halo events. Furthermore, to veto beam-gas events (when an accelerated heavy-ion strikes a residual gas molecule), a coincidence of signals at MBTS and ZDCs was required. These are the standard heavy ion settings utilized by other analyses as well, see e.g. [49].

To conclude, Table 4.1 summarizes the dataset names and numbers of events.

Description	Dataset name	# events
MB 2011 Pb+Pb	data11_hi.00*.physics_MinBias.merge.NTUP_HI*p1253_p1270	42.287 M
	data11_hi.00*.physics_HardProbes.merge.NTUP_HI*p1238_p1249	
HP 2011 Pb+Pb	data11_hi.00*.physics_HardProbes.merge.NTUP_HI*p1253_p1270	14.156 M
	data11_hi.00*.physics_HardProbes.merge.NTUP_HI*p1281_p1270	

Table 4.1: Summary of data used in the analysis

4.1.2 Monte Carlo reference

In order to simulate the jet events in realistic conditions of heavy ion collisions, the PYTHIA di-jet events were embedded into real minimum-bias heavy-ion collisions measured during 2011 data taking. The detector response to each event was individually simulated using a full GEANT4 [50] description of AT-LAS [51]. The overlay of PYTHIA to real data was done at the digitization level. These events thus contain, both the reconstructed quantities (e.g. tracks, calorimeter jets) and PYTHIA particle level information which is called "truth" (truth particles and truth jets).

We used three sets of PYTHIA MC samples (J3 – J5 samples). Each of them has a fixed range of transverse momenta in the PYTHIA hard scattering. For this analysis the different J samples were combined using a cross-section weighing to obtain a combined sample with good statistics over a wide range of jet $\hat{p}_T$ (the transverse momentum of outgoing partons in the $2 \to 2$ hard-scattering). The names of PYTHIA samples and their respective numbers of events can be found in Table 4.2. The definitions of p_T ranges and the associated cross-sections are shown in Table 4.3. The MC samples were subjected to the same event selection as the Minimum Bias data which is described in the previous section.

J	Dataset name	# events
3	mc11_2TeV.105012.J3_pythia_jetjet.recon.NTUP_HI.e1296_d724_r4789	4.531 M
4	mc11_2TeV.105013.J4_pythia_jetjet.recon.NTUP_HI.e1296_d724_r4789	4.535 M
5	mc11_2TeV.105014.J5_pythia_jetjet.recon.NTUP_HI.e1296_d724_r4789	4.5536 M

Table 4.2: Names of the PYTHIA J samples.

J	$\hat{p}_\mathrm{T}^\mathrm{min}$ [GeV/c]	$\hat{p}_\mathrm{T}^\mathrm{max}$ [GeV/c]	σ [nb]
3	70	140	294.17
4	140	280	6.4489
5	280	560	0.063882

Table 4.3: Definitions of embedded PYTHIA dijet.

4.1.3 Centrality definition and determination

The collision centrality can be intuitively thought of as the degree of overlap of the two colliding nuclei. It is one of the most important factors in heavy-ion physics, because the system produced in the most overlapping heavy-ion collisions is expected to create the best conditions necessary for the QGP production. In other words, closer the collision is to "head-on" (we say the collision is more "central"), the more likely plasma production will be. On the other hand, more "peripheral" collisions are less likely to create ideal conditions for the plasma production [17].

In ATLAS, the PbPb collision centrality is characterized using the summed transverse energy ($\sum E_\mathrm{T}$) deposited in the forward calorimeters (FCal). The minimum bias FCal $\sum E_\mathrm{T}$ distribution of the data analyzed in this work is illustrated in Figure 4.1. The FCal $\sum E_\mathrm{T}$ is used for this analysis to avoid biasing the centrality measurements by jets, which are produced with the highest probability in the barrel region [35].

The shape of the energy distribution (Figure 4.1) can be explained very intuitively. The more frequent peripheral collisions with large impact parameter produce only few particles, which generate only a small response in FCal (the left end of the distribution), while the rare central collisions with small impact parameter generate many more particles because of the increased number of nucleon-nucleon interactions (the right end of the distribution).

For the purpose of this analysis, the fine-grained bins on Figure 4.1 were combined into 10 larger bins, which are defined according to fractions of the total PbPb cross section in minimum bias events. These bins are expressed in terms of percentiles. By convention, the $0-10\%$ bin represents the 10% most central events (highest values of FCal $\sum E_\mathrm{T}$) and increasing percentiles refer to events with successively lower FCal $\sum E_\mathrm{T}$ and thus successively smaller centrality. The Table 4.4 contains values of FCal $\sum E_\mathrm{T}$, which determine different centrality bins, together with the mean values $\langle\mathrm{FCal}\ \sum E_\mathrm{T}\rangle$ [52].

Figure 4.2 confirms the assumption that various centrality bins contain, by definition, the same amount of minimum bias events.
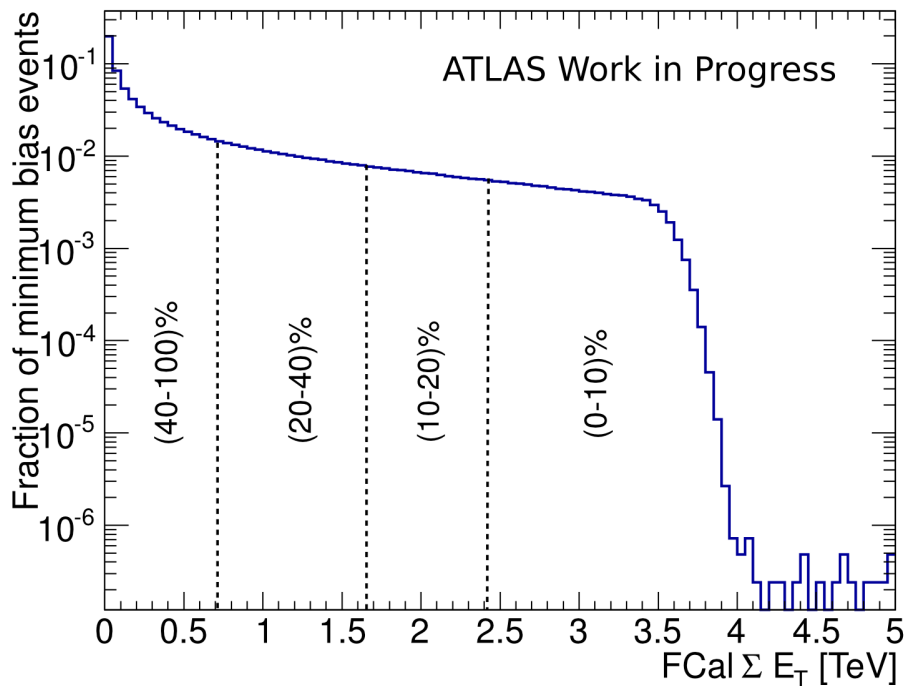
Figure 4.1: Probability distribution of $\sum E_T$ in the forward calorimeters for minimum bias data. The four regions of centrality are indicated by dashed lines and labeled according to increasing fraction of lead-lead total cross section. Central collisions (0-10%) deposit large amounts of energy in the FCal while peripheral (40-100%) have small energy deposits.

Centrality	FCal $\sum E_T$ range [TeV]	$\langle$FCal $\sum E_T\rangle$ [TeV]
$0-10\%$	> 2.423	2.903
$10-20\%$	$2.423 - 1.661$	2.033
$20-30\%$	$1.661 - 1.116$	1.363
$30-40\%$	$1.116 - 0.716$	0.885
$40-50\%$	$0.716 - 0.430$	0.545
$50-60\%$	$0.430 - 0.239$	0.308
$60-70\%$	$0.239 - 0.119$	0.160
$70-80\%$	$0.119 - 0.053$	0.077
$80-90\%$	$0.053 - 0.019$	0.032
$90-100\%$	< 0.019	-

Table 4.4: Values of FCal $\sum E_T$ and $\langle$FCal $\sum E_T\rangle$ for the centrality bins used in this analysis.
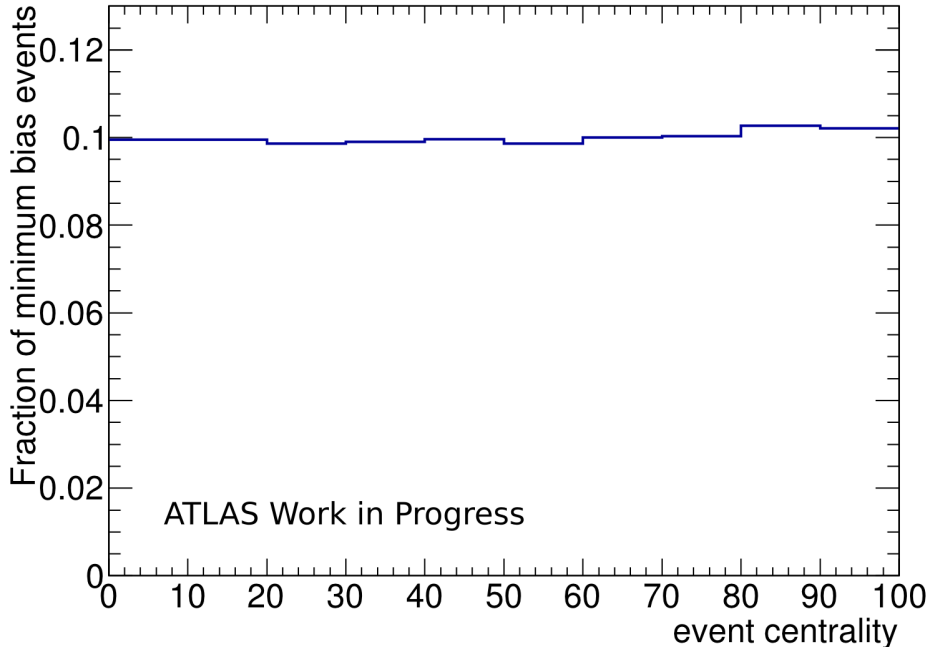
Figure 4.2: Distribution of the fraction of events in ten centrality bins. The centrality-bin labels run from 0% (most central events) to 100% (most peripheral events).

4.2 Definition and General Behavior of the Missing Transverse Momentum

The law of conservation of momentum dictates that the total sum of transverse momenta vectors $\mathbf{p}_T$ of all the particles created in the collision should be zero[1]:

$$\mathbf{p}_T = \sum_{i=0}^{N} \mathbf{p}_{T,i} = \mathbf{0}, \qquad (4.1)$$

where i is the integer labeling the particle and N is the total number of particles produced in the collision (i.e., the multiplicity of the collision). In other words, the $\mathbf{p}_T$ vector calculated by adding the $\mathbf{p}_{T,i}$ vectors of individual particles produced in an event should be a zero vector.

This fact is, however, almost never observed in real experiments. We can, therefore, talk about a *missing transverse momentum vector* $\not{\mathbf{p}}_T$ (in the rest of this work this quantity will be referred to without boldface notation, i.e. $\not{p}_T$). This observable is of high importance when studying the phenomenon of jet quenching. It is usually calculated by adding the momenta vectors of all reconstructed ID tracks present in an event vectorially and multiplying this by -1, as

---

[1] The summation sign here denotes the vector sum.

defined in the following equation:

$$\not{p}_\text{T} \equiv - \sum_{i=0}^{N} \mathbf{p}_{\text{T},i} = -\mathbf{p}_\text{T}.$$ (4.2)

A nonzero $\not{p}_\text{T}$ in an event usually has contributions from many sources. The primary source of $\not{p}_\text{T}$ are neutrinos, which are produced in weak interactions and which escape from collider detectors without producing any direct response in the detector elements. The presence of such particles must be deduced from the overall imbalance of the total momentum [53]. Another contributions to $\not{p}_\text{T}$ include measurement resolutions, instrumental defects in the detector system, and reconstruction inefficiencies. Apart from the undetected particles, these contributions are considered unwanted, because they distort the measurements.

4.2.1 Toy Monte Carlo

Before we started the analysis of ATLAS data and Monte Carlo (MC) events a simple "toy" Monte Carlo simulation has been performed. The main purpose of this simulation was to define $\not{p}_\text{T}$ and to explore the basic properties of this quantity under idealized conditions.

This MC was based on random number generation. It created a set of N_C "virtual" collisions, each with a different number of particles, N_p. The total number of particles in each collision was uniformly distributed from $N_{\text{p,min}}$ to $N_{\text{p,max}}$. Every particle in an event was assigned a value of $p_{\text{T},i}$ and an azimuthal angle ϕ_i. The values of ϕ_i were uniformly distributed over the interval $[-\pi, \pi]$. The number of particles carrying the transverse momentum p_T, $N(p_\text{T})$, followed the exponential distribution:

$$N(p_\text{T}) = ae^{-b \cdot p_\text{T}},$$

where a and b are free parameters chosen to be 1 and 5, respectively. Note that the behavior of quantities discussed further (especially of $\not{p}_\text{T}$) does not depend on the choice of these parameters.

Using the value of $p_{\text{T},i}$ and angle ϕ_i we calculated the x and y components of the transverse momentum of a given particle i using simple formulae:

$$p_{\text{T},i}^\text{x} = p_{\text{T},i} \cdot \cos\phi_i,$$ (4.3)
$$p_{\text{T},i}^\text{y} = p_{\text{T},i} \cdot \sin\phi_i.$$ (4.4)

For every event the values of p_T^x and p_T^y of every particle were summed to obtain the final vector $\mathbf{p}_\text{T}$. The magnitude of this vector reads as:

$$p_\text{T} = \sqrt{\left(\sum_i p_{\text{T},i}^\text{x} \right)^2 + \left(\sum_i p_{\text{T},i}^\text{y} \right)^2}.$$ (4.5)

The vector $\not{p}_T$ is, according to the Equation (4.2), just the vector of $\mathbf{p}_T$ with the minus sign. Thus they both have equal magnitude.

The individual x and y components of $\not{p}_T$ can, therefore, be calculated as:

$$\not{p}_T^x = -\sum_i p_{T,i}^x, \tag{4.6}$$

$$\not{p}_T^y = -\sum_i p_{T,i}^y. \tag{4.7}$$

These are the quantities we will thoroughly discuss throughout the rest of the thesis.

The values of parameters used in this simulation were: $N_C = 100,000$; $N_{p,\min} = 10$ and $N_{p,\max} = 6,000$. Each event was assigned to one of six bins according to the number of particles in the event, that is, according to the "activity" of the collision. In real collisions the activity of the event reflects the centrality of the collision, which is a crucial quantity in the heavy-ion physics and which was introduced in Sections 1.4 and 4.1.3.

The distribution of $\not{p}_T$ for each of these bins is displayed in Figure 4.3. The horizontal axis in this figure does not have an associated unit for the $\not{p}_T$, because we are only interested in the qualitative behavior of the distribution. Histograms are normalized according to the number of entries in each activity bin.
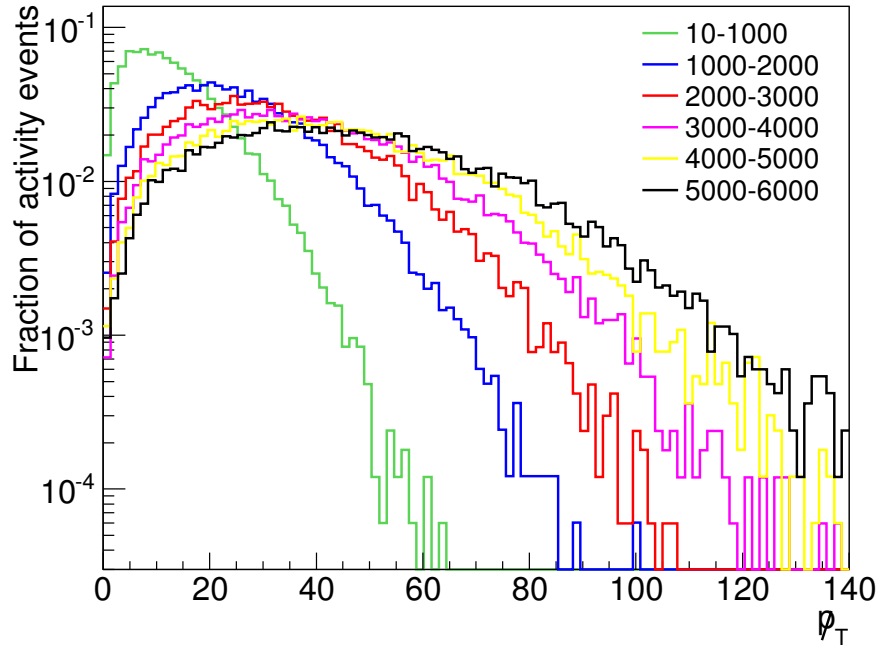

Figure 4.3: Probability distribution of $\not{p}_T$ for six activity bins in MC toy simulation.

Let us now introduce one more quantity regarding $\not{p}_T$, the *missing p_T significance* $\not{p}_T^{\mathrm{sign}}$, which is often used in the studies of the missing p_T and shall help us

to understand the behavior of missing p_T. It is defined for each collision as $\not{p}_T$ divided by the square root of the total transverse momentum of all the particles in that collision:

$$\not{p}_T^{\text{sign}} = \frac{\not{p}_T}{\sqrt{\sum_i p_{T,i}}}. \tag{4.8}$$

In an idealized case of our MC simulation, the distribution of $\not{p}_T^{\text{sign}}$ should be the same for each centrality bin. This is really the case, as shown in Figure 4.4. The reason for this will be explained in the following paragraphs.
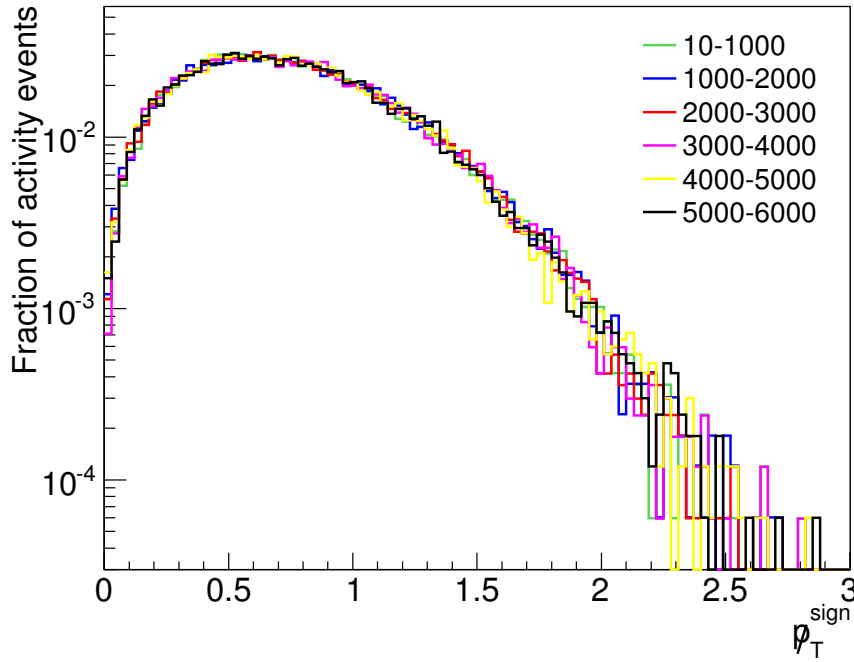
Figure 4.4: Probability distribution of $\not{p}_T^{\text{sign}}$ for six activity bins in MC toy simulation.

Looking at the Figures 4.3 and 4.4, one could wonder about the origin of the $\not{p}_T$. Remember that this is just a toy MC simulation, without any implemented mechanism, which would generate the missing transverse momentum of the simulated collisions. As it turns out, this $\not{p}_T$ stems from finite statistics of particles we are dealing with. In order to understand this, imagine the transverse plane of the detector as a circle. Let us now generate N_p particles with uniformly distributed ϕ and divide the transverse plane in two halves, each spanning π in azimuth (for example, the upper half of the detector $\phi \in (0, \pi)$ and the bottom half $\phi \in (\pi, 2\pi)$). Say that the number of particles with azimuthal angle belonging to the upper half of the detector is N, and number of the remaining particles (those hitting the bottom half) is M (obviously, $M + N = N_p$).

The overall $\not{p}_T$ can be approximated using the mean particle transverse momentum $\langle p_T \rangle$:

$$\not{p}_T \approx \langle p_T \rangle M - \langle p_T \rangle N = \langle p_T \rangle (M - N). \tag{4.9}$$

The uncertainty of this quantity can be evaluated as the error of the indirect

measurement:

$$(\delta \not{p}_\mathrm{T})^2 = \left(\frac{\partial \not{p}_\mathrm{T}}{\partial M}\right)^2 (\delta M)^2 + \left(\frac{\partial \not{p}_\mathrm{T}}{\partial N}\right)^2 (\delta N)^2 = \langle p_\mathrm{T} \rangle^2 (M + N), \qquad (4.10)$$

where δM and δN are the uncertainties of M and N, respectively. The last equality follows from the fact that the standard deviation of the Poisson process is the square root of the number of entries.

One can see that the error of the measurement of missing p_T is proportional to the square root of p_T sum:

$$\langle p_\mathrm{T} \rangle \sqrt{M + N} \sim \sqrt{\sum_i p_{\mathrm{T},i}}. \qquad (4.11)$$

Hence, the significance of the missing p_T is missing p_T scaled by its error, which is the reason why we see the scaling in Figure 4.4 and which also confirms the explanation of the origin of the missing p_T in our toy MC: $\not{p}_\mathrm{T}$ stems from finite statistics of particles we are dealing with.

This toy MC does not bring any new knowledge, but helps us to understand the basic behavior of missing p_T and its origin. In the following sections we will explore the missing p_T in the context of jet measurements using PYTHIA MC samples and real data collected by ATLAS.

4.3 Basic Cuts and Corrections

4.3.1 Cuts for particles and jets

The lower threshold for the transverse momenta of particles considered in this analysis was set to $p_\mathrm{T}^\mathrm{thrs} = 0.5$ GeV/c and since the Inner Detector (ID) covers the $|\eta| < 2.5$ only tracks within this pseudorapidity interval can be considered. The requirements for the selection of quality tracks consist of cuts on number of hits in different subdetectors of ID and cuts on the pointing of tracks to the primary vertex. The longitudinal (z_0) and transverse (d_0) impact parameter of the track measured with respect to the primary vertex are scaled by their errors (z_0^{cov}, d_0^{cov} and $\sin \theta^{cov}$) which defines a significance of the impact parameter (σ_{z_0} and σ_{d_0}). The full list of track-quality selection requirements is then:

- at least two hits in the Pixel ID

- at least seven hits in the Semiconductor Tracker (SCT)

- at least one hit in the first layer of the Pixel ID (BLayer) if expected

- $\sigma_{z_0} \equiv \dfrac{z_0 \sin \theta}{\sqrt{z_0^{cov} \sin^2 \theta + \sin \theta^{cov} (z_0 \sin \theta)^2}} < 3; \qquad \sigma_{d_0} \equiv \dfrac{d_0}{\sqrt{d_0^{cov}}} < 3$

These cuts were found to provide a selection of tracks with a minimum contribution from mis-reconstructed tracks while keeping the tracking efficiency at a high level.

Jets have been reconstructed using the anti-k_t jet clustering algorithm [31] with the radius parameter $R = 0.4$. It is the standard jet algorithm used by both ATLAS [35], and CMS [22]. The transverse energy of the jet is equal to the sum of the transverse energies deposited in calorimeters belonging to the reconstructed jet cone. The average contribution from the underlying event to the jet was subtracted. Moreover, axis of the jet was required to lie within the pseudorapidity range of $|\eta| < 2.1$ in order to capture all particles within a jet cone.

4.3.2 Corrections for the components of missing p_{T}

To investigate the basic behavior of $\not{p}_{\mathrm{T}}$, similar analysis to the one presented in Section 4.2.1 has been made on minimum bias data. The distributions of $\not{p}_{\mathrm{T}}$ and $\not{p}_{\mathrm{T}}^{\mathrm{sign}}$ for centrality bins defined in the previous section are shown in Figures 4.5 and 4.6. The $(80-100)\%$ centrality bin is omitted, because it comprises only the most peripheral collisions, which are not of much interest. Note that the distributions displayed in these figures, as well as in the rest of this work, are normalized according to the number of events in the given centrality bin.
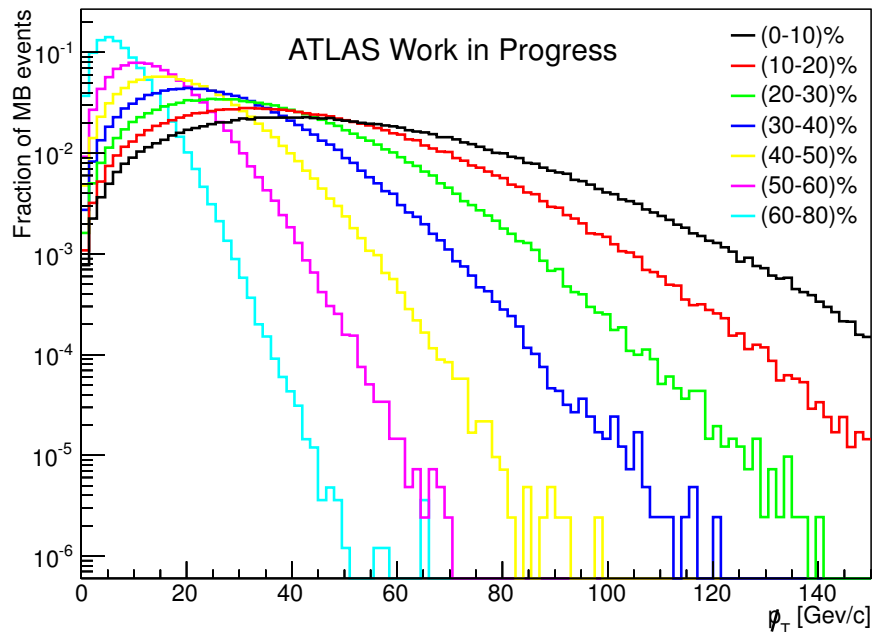

Figure 4.5: Probability distribution of $\not{p}_{\mathrm{T}}$ for seven centrality bins.

As we can observe, the qualitative behavior of the missing transverse momentum and its significance is almost identical to the ones for toy MC. However, there may be some small differences caused by the malfunctioning regions in ID, which distort the missing p_{T}, as will be shown in the following text.
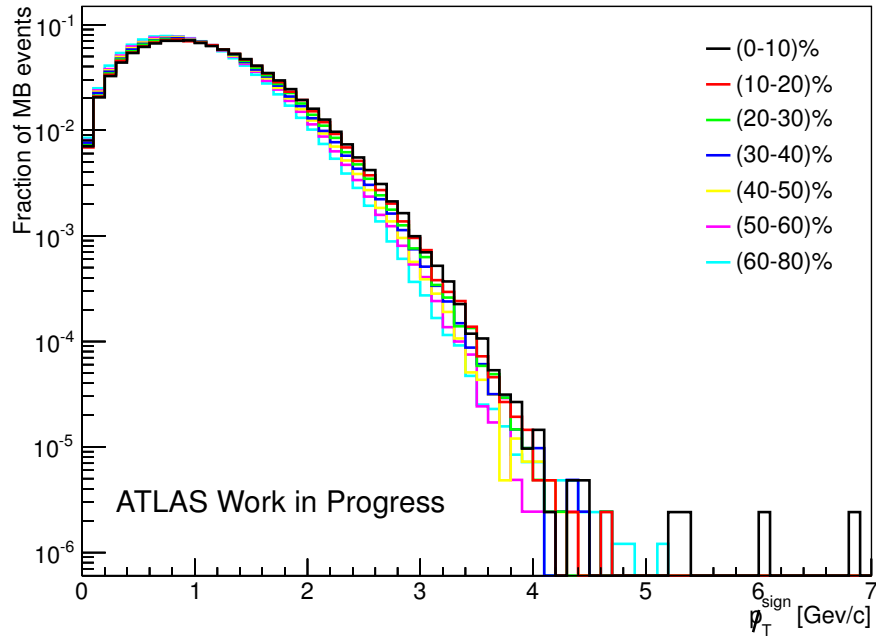
Figure 4.6: Probability distribution of $\not{p}_\mathrm{T}^\mathrm{sign}$ for seven centrality bins.

As already mentioned, some of the missing p_T may be generated due to the presence of faults in ATLAS ID system. We shall demonstrate this effect on a simple example. For the sake of simplicity, let us consider the extreme case where one half of the Inner Detector is completely dysfunctional, for example all of the detectors in the range of $\phi \in (0, \pi)$ (that is, the upper half of the detector). If we were now to measure transverse momenta of a huge amount of particles, the overall $\not{p}_\mathrm{T}$ would be pointing upwards (towards the faulty parts of the Inner Detector), because no particles have been detected in the range $\phi \in (0, \pi)$.

It is therefore useful to create the "map" of the detector, which would display the faulty spots in the tracking system. This can be done by plotting the density of tracks emerging from minimum bias collisions with $p_\mathrm{T} > 0.5 \ \mathrm{GeV/c}$ in two dimensional $\eta \times \phi$ space. This is illustrated in Figure 4.7.

The natural segmentation in η does not concern us, since the missing p_T projection does not depend on the overall η dependence of the underlying event as one can infer from equations mentioned in Section 4.2. The inhomogeneity in ϕ, however, has a significant impact on the analysis, because it distorts the calculations of $p_{\mathrm{T},i}^\mathrm{x}$ and $p_{\mathrm{T},i}^\mathrm{y}$.

Let us now look at the consequences of these faults on the $\not{p}_\mathrm{T}$ in Hard Probe stream events. They can be observed in Figures 4.8 and 4.9. These graphs show the values of means of the distributions of x and y components of $\not{p}_\mathrm{T}$. If the tracking system of the ID was flawless these distributions would be zero-centered and their means would be centrality independent. This is almost true for the y component but does not appear to hold for the x component. Since
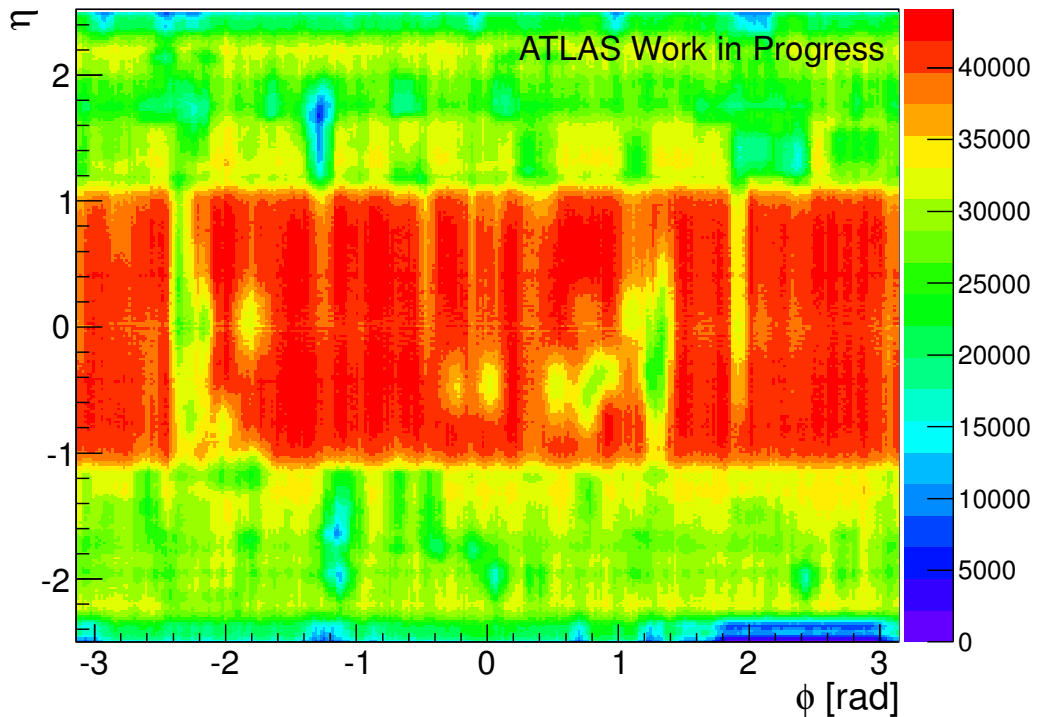
Figure 4.7: Scatter plot illustrating the number of tracks in $\eta \times \phi$ phase space. Color indicates the density of the tracks and is given in numbers, representing the amount of tracks in 0.01×0.02 bins of $\eta \times \phi$ space.

the $\not{p}_T$ is a basic observable of this analysis, our main concern is to reduce the centrality dependence of these observables.

In the rest of this work the analyses shall be done for four individual particle p_T ranges: $(0.5 - \infty)$ GeV/c, $(0.5 - 2)$ GeV/c, $(2 - 4)$ GeV/c, $(4 - \infty)$ GeV/c which reflect the selection in the original study of missing p_T done by CMS [22].

The first correction that we can apply is the correction for the tracking efficiency. This correction works as follows: first we take the map of particle tracks displayed in Figure 4.7, then we do the projection on the η axis and normalize it according to the number of ϕ bins and, finally, we divide each ϕ slice of the track map by this projection. What we are left with is a two-dimensional histogram displayed in Figure 4.10.

As one can see from the figure, this histogram contains values fluctuating around 1. If we now multiply the momentum of each particle going into specific $[\eta, \phi]$ direction by the inverse of the histogram value at this coordinate we effectively eliminate the detector effects on the overall missing p_T vector in an event. To what extent is this method effective can be seen in Figures 4.11 and 4.12 which show the mean values of missing p_T components in the HP stream as a function of collision centrality after applying the aforementioned correction.

Apparently this correction helped to shift the means of histograms of missing p_T vector components towards zero mainly for the $(0.5 - \infty)$ and $(0.5 - 2)$ p_T
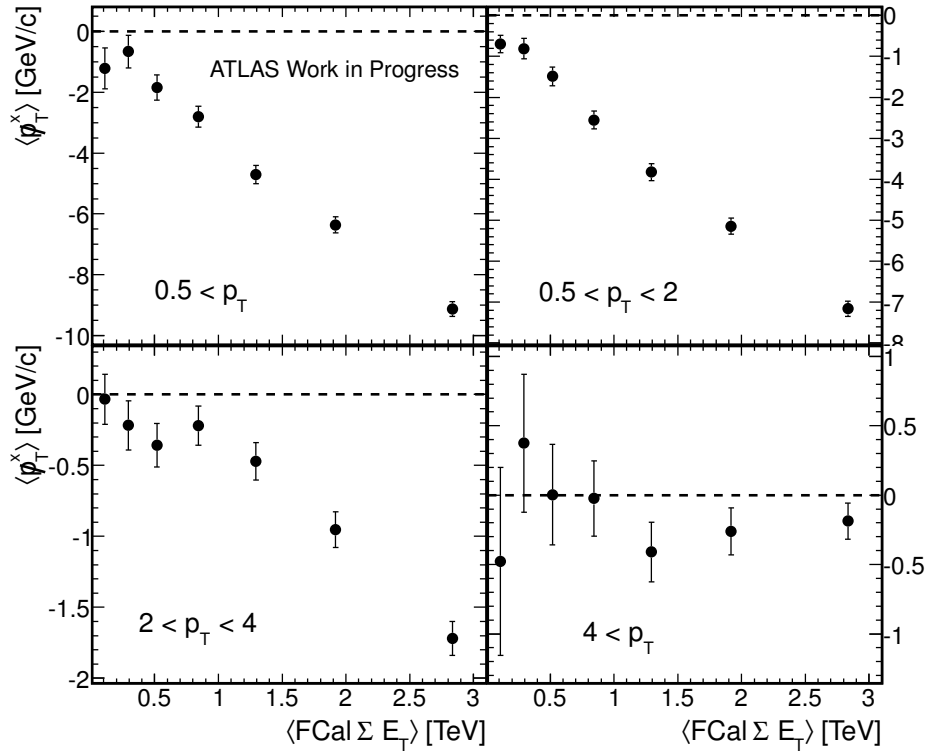
Figure 4.8: The centrality dependence of the average missing transverse momentum in the x direction for four individual p_T ranges.
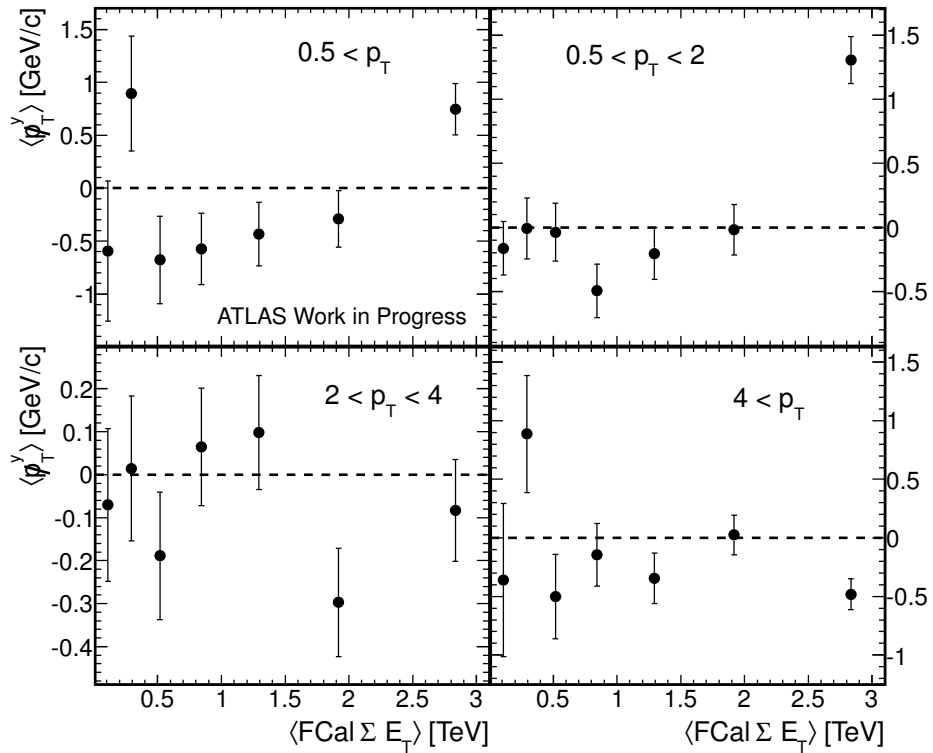

Figure 4.9: The centrality dependence of the average missing transverse momentum in the y direction for four individual p_T ranges.
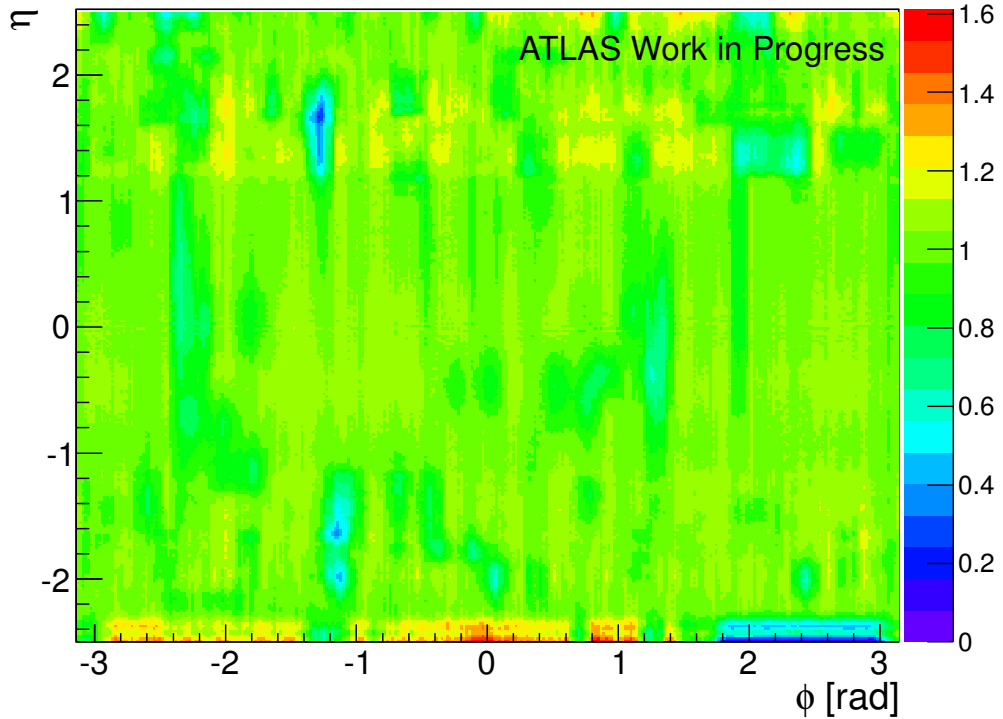
Figure 4.10: Map of the inverse of the track momentum weights. Value of 1 means no track p_T correction is applied for particles going into this coordinate of the ID.

bins of the x component.

It is now possible to use values reported in Figures 4.11 and 4.12 to define an additive correction which removes the remaining centrality dependence of components of $\not{p}_T$ vector and sets their mean values to zero. This additive correction subtracts the mean values reported in Figures 4.11 and 4.12 from missing p_T components calculated in each event during the analysis. The resulting distribution of components of $\not{p}_T$ vector are summarized in Figures 4.13 and 4.14. These figures show that the mean value is centered at zero for each centrality bin and they also demonstrate the deterioration of the missing p_T resolution with increasing centrality. Same procedure as described in this section was applied also during the analysis of reconstructed Monte Carlo data. The efficiency map presented in Figure 4.10 was in that case defined using the simulation data to avoid small differences between the simulation of the detector response in MC and in the real data.
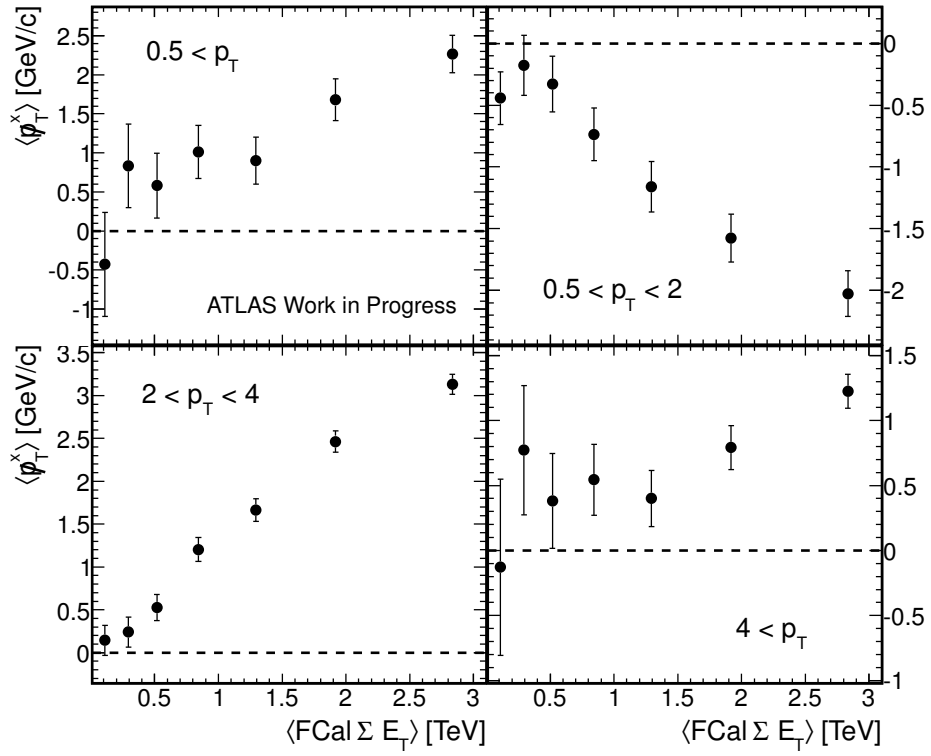
Figure 4.11: The centrality dependence of the average missing transverse momentum in the x direction for four individual p_T ranges after the correction.
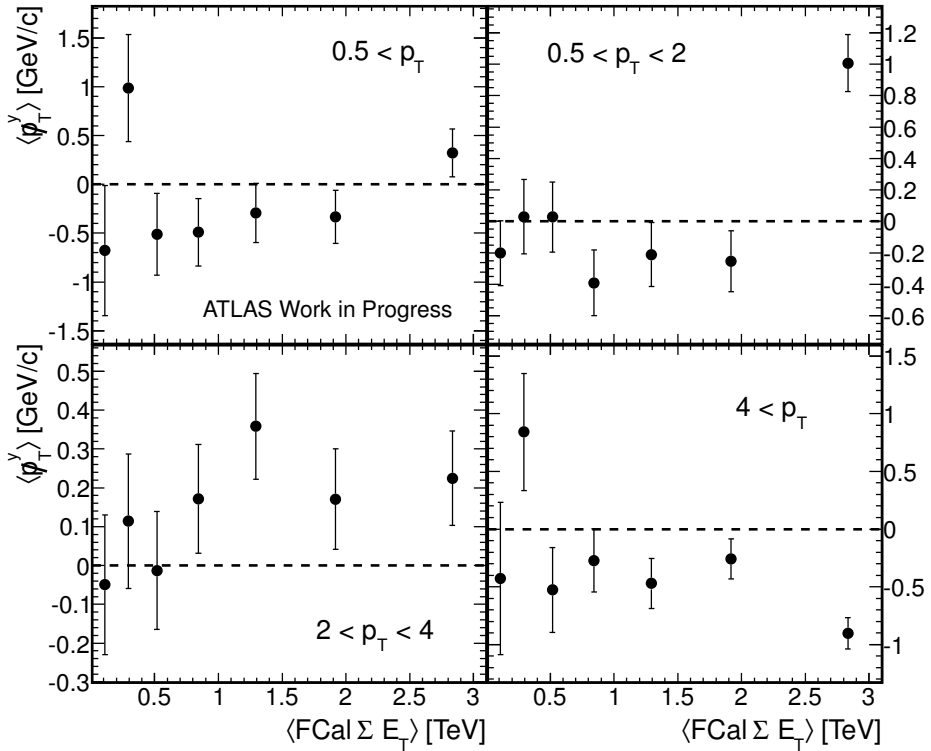

Figure 4.12: The centrality dependence of the average missing transverse momentum in the y direction for four individual p_T ranges after the correction.
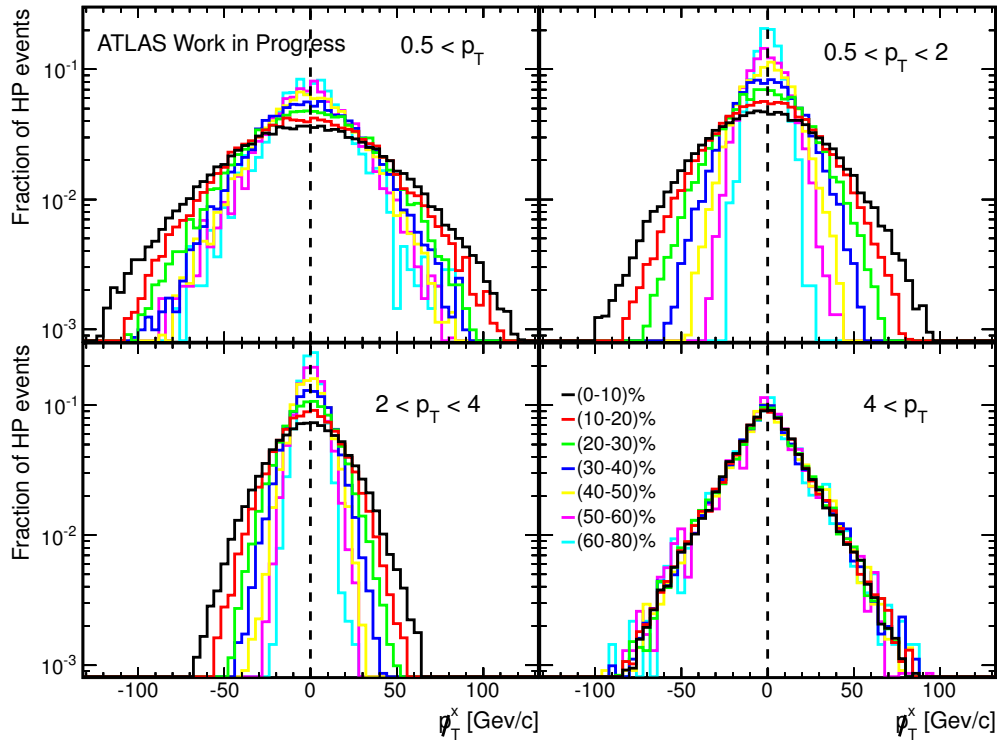
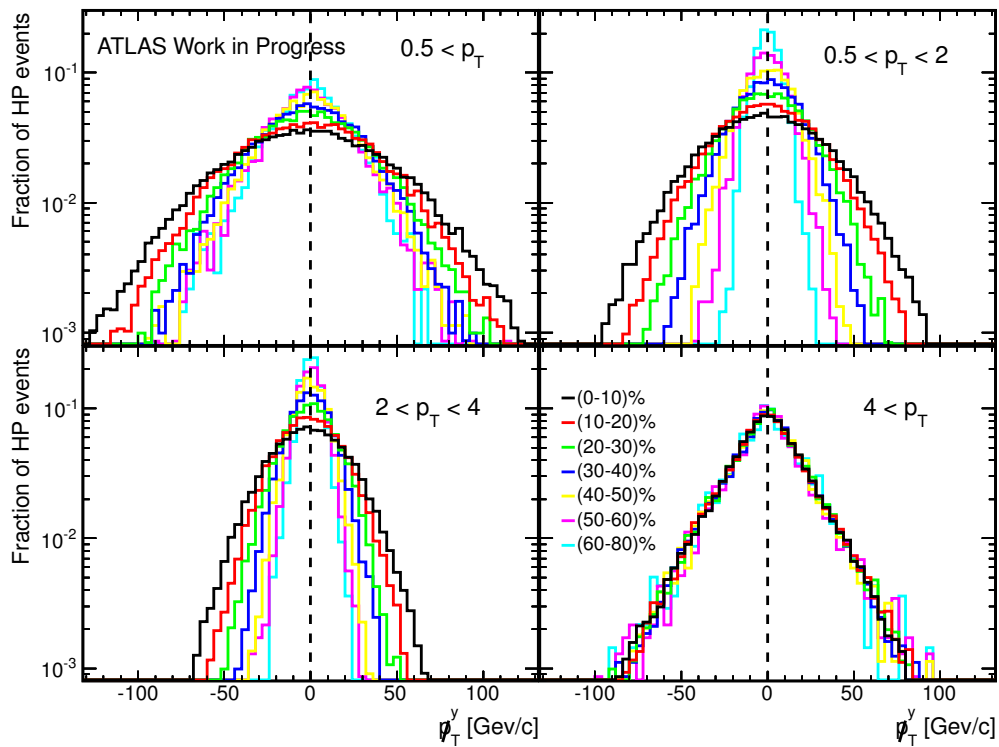Figure 4.13: Probability distributions of the corrected x component of $\not{p}_T$ vector for four individual p_T ranges.

Figure 4.14: Probability distributions of the corrected y component of $\not{p}_T$ vector for four individual p_T ranges.

4.3.3 Corrections of jets

The underlying event subtraction which is performed during the jet reconstruction leaves jets that are not calibrated. Jet calibration needs to be applied in order to correct e.g. for differences in the detector response to the electromagnetic part and hadronic part of the calorimeter shower. This correction is done using standard ATLAS calibration. Further, the jets are corrected for a presence of correlated background fluctuations by matching the jets to electromagnetic clusters and to jets reconstructed in the ID. The jets used in this study reach a fully efficiency at about 90 GeV.

Chapter 5

Analysis of Data and Monte Carlo

The measurements presented in the following sections aim to characterize the energy loss mechanism that is responsible for the energy "lost" in the subleading jet compared to the leading jet in highly unbalanced dijet pairs. In order to accomplish this task, we study the differences in the redistribution of the "lost" energy by the leading and subleading jet as a function of transverse momentum. The distributions are extracted for several selections of PbPb collision centrality both in real data and PYTHIA MC simulations. Finally, these distributions are studied for different selections of dijet asymmetry A_{J}.

5.1 Dijet Asymmetry

The basic condition for the offline selection of events is described in Section 4.1.1. On top of these conditions, a presence of two jets in the pseudorapidity range of $|\eta| < 2.1$ (to capture all particles within a jet cone) is required. The transverse energy of the leading jet (the jet with the highest transverse energy) labeled as E_{T1} is required to be $E_{\mathrm{T1}} > 100$ GeV, and the subleading (next to the highest transverse energy) jet has to have $E_{\mathrm{T2}} > 25$ GeV. The azimuthal angle between the leading and subleading jets is required to be $\Delta\phi = |\phi_1 - \phi_2| > 2\pi/3$. This requirement is used to reduce contributions from multi-jet final states. These settings were adapted from the paper [35]. By selecting leading jets with rather large transverse energies we ensure full reconstruction efficiency. The requirement for the subleading jet assures that this jet is reliably detected above the underlying event.

It is important to characterize the dijet energy balance (or imbalance) with a single quantity. To do so, the dijet asymmetry, A_{J}, is introduced:

$$A_{\mathrm{J}} = \frac{E_{\mathrm{T1}} - E_{\mathrm{T2}}}{E_{\mathrm{T1}} + E_{\mathrm{T2}}},\tag{5.1}$$

where the subscripts 1 and 2 refer to the leading jet and subleading jet, respectively. This construction ensures that A_{J} is always positive and reduces uncertainties caused by possible constant shifts of the jet energy scale. Regular dijet

events are expected to have the A_J distribution dominated by the contribution at zero. The deviations from zero are caused by a combination of intrinsic properties of dijets and the jet energy resolution. Energy loss caused by the propagation through the dense medium is expected to produce strong deviations in the reconstructed energy balance. This was indeed observed in [22, 35].

It is important to note that the $E_{\mathrm{T}2}$ threshold of 25 GeV constrains the $E_{\mathrm{T}1}$-dependent limit on the magnitude of A_J. For the most common leading jets with energies just above the 100 GeV threshold, this limit is $A_\mathrm{J} < 0.41$. The largest possible value of the dijet asymmetry ratio for the used dataset is $A_\mathrm{J} = 0.77$ for the highest energy leading jets with $E_{\mathrm{T}1} \approx 400$ GeV. Jets carrying the energy of this magnitude are, however, very rare, and we can consider $A_\mathrm{J} = 0.7$ as an effective upper limit of the energy imbalance, when exploring event properties differentially in the dijet asymmetry.

The example of the dijet asymmetry distribution is shown in Figure 5.1. The figure compares A_J distributions reconstructed in $0 - 10\%$ and $60 - 80\%$ centrality bins in Monte Carlo (MC) and in data. One can indeed see larger contribution of events with imbalanced dijets in the data compared to MC in the central collisions. The full details of the analysis of the MC sample and data sample is presented in the next sections.
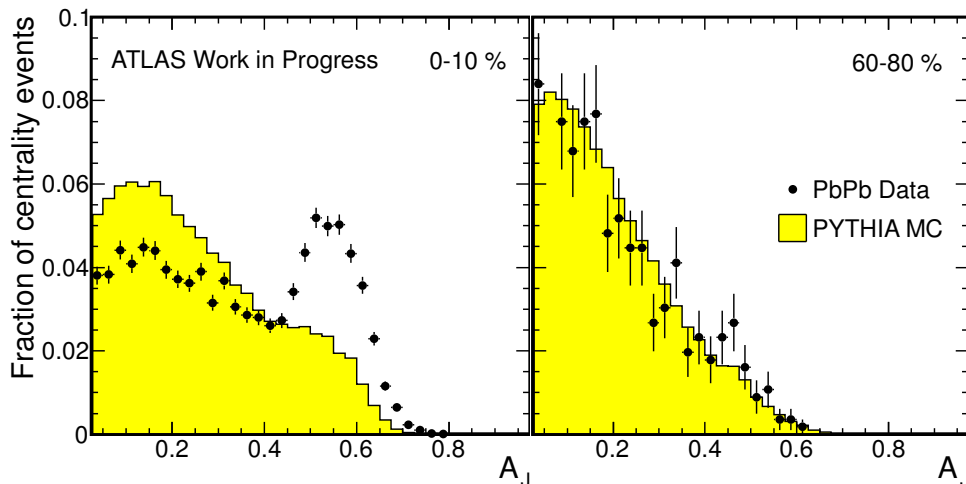

Figure 5.1: A_J distributions for data (points) and PYTHIA MC (solid yellow histograms) for central (left panel) and peripheral (right panel) PbPb collisions.

5.2   Analysis of Monte Carlo Reference Sample

The MC analysis has been performed both at the truth particle level and at the reconstructed level containing a simulation of the detector. For the analysis at the reconstructed level, we applied the cuts and corrections described in detail in Section 4.3. The MC data samples and event selection criteria are described in Section 4.1.2.

The missing p_T projections that are main observables of this analysis were unfolded (that is corrected from the reconstructed to the truth level) by the bin-by-bin correction as discussed later in this section.

Before we present the study of energy imbalance, it is useful to explore the angular behavior of the missing transverse momentum evaluated with respect to the jet position. More precisely, the object of our interest is the angle between the missing momentum vector $\not{p}_\mathrm{T}$ and the axis of leading jet defined in Section 3.2. Hence, we introduce angular differences α defined as:

$$\alpha_\mathrm{LJ} = |\phi_\mathrm{MPT} - \phi_\mathrm{Leading\ Jet}|, \tag{5.2}$$

where ϕ_MPT is the azimuthal angle of $\not{p}_\mathrm{T}$. The behavior of the quantity α_LJ is shown in Figure 5.2 for the truth MC and in Figure 5.3 for the reconstructed MC. To enhance the readability of figures angular distributions of only four (out of total seven) centrality bins are displayed.
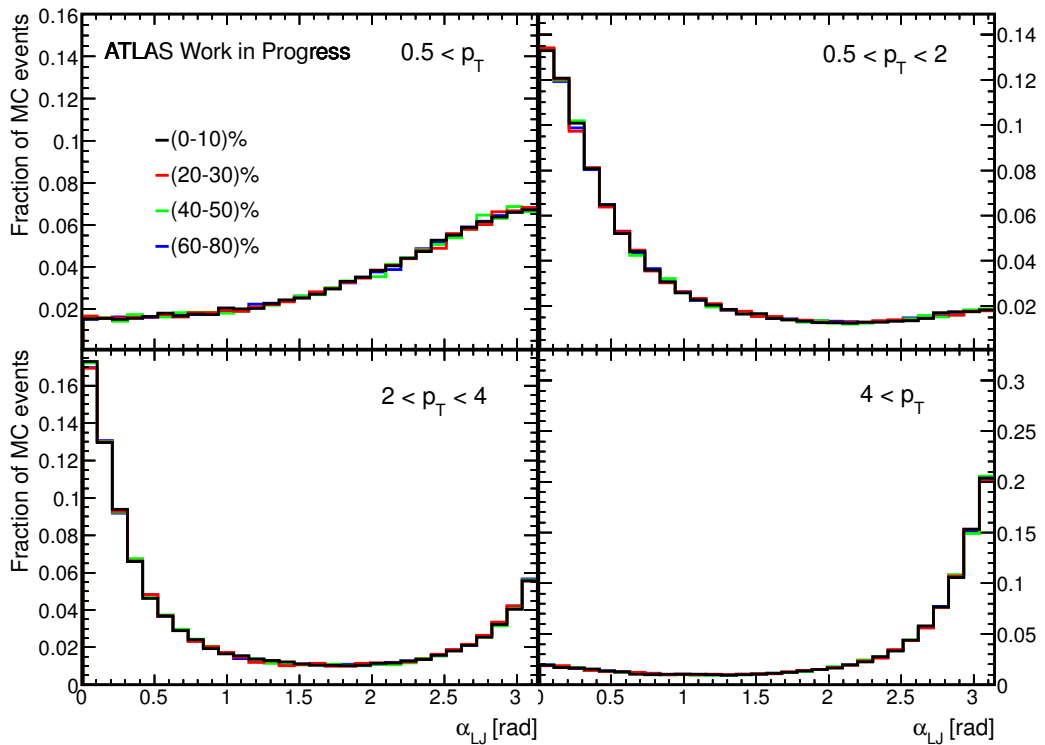

Figure 5.2: Probability distributions of the angle between the $\not{p}_\mathrm{T}$ vector and leading jet axis for four individual p_T ranges in truth Monte Carlo events.

The first feature obvious from these plots is the fact that there is absolutely no centrality dependence in the MC truth. This is, of course, expected since the truth MC deals only with particles generated from pQCD calculations without any sort of jet quenching mechanism. There is also no detector present in truth MC which would distort these measurements. The basic properties seen in Figure 5.2 are following. For the highest p_T particles ($p_\mathrm{T} > 4$ GeV/c), we can see that the $\not{p}_\mathrm{T}$ points dominantly to the direction of the subleading jet (e.g.,
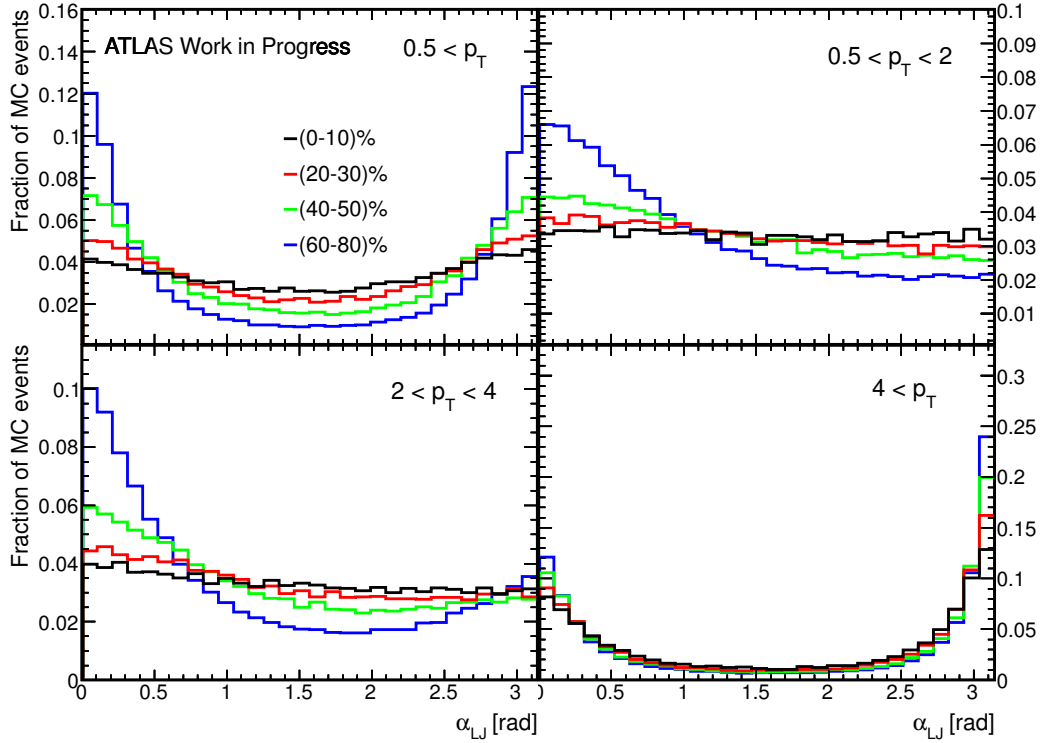
Figure 5.3: Probability distributions of the angle between the $\not{p}_T$ vector and leading jet axis for four individual p_T ranges in reconstructed Monte Carlo events.

α_{LJ} near π for the bottom right panel in both figures), which reflects the fact that the subleading jet has less particles with high-p_T than the leading jet. For the low-p_T particles $(0.5 - 4\ \mathrm{GeV/c})$ the $\not{p}_T$ points dominantly to the leading jet (e.g., α_{LJ} near 0 in Figure 5.2), which is a consequence of subleading jet having more low-p_T particles than the leading jet.

In the reconstructed MC sample there is an obvious centrality dependence caused by the detector effects namely the jet position and energy resolution and tracking efficiency which play a more important role in central collisions, compared to peripheral collisions. The jet energy resolution not only smears the jet energies, it may also lead to a misidentification of the leading jet as subleading jet and vice versa. This leads to the observed enhancement of yields at zero angles for the hardest particles.

It is not easily possible to disentangle the underlying physics from these figures, since jets with different A_J contribute simultaneously to the distributions of α_{LJ}. Moreover, the magnitude of the missing transverse momentum varies in a given centrality bin according to the physics, as we shall further see.

To get some information about the overall energy balance (or imbalance) of dijet events, we can use the projections of $\not{p}_T$ vector of reconstructed tracks onto the axis of leading jet. These were calculated for each event as the scalar

projections:

$$p\!\!\!/_{\mathrm{T}}^{||,\mathrm{LJ}} = p\!\!\!/_{\mathrm{T}} \cos \alpha_{\mathrm{LJ}}, \tag{5.3}$$

where $p\!\!\!/_{\mathrm{T}}$ is the magnitude of the missing transverse momentum vector and α_{LJ} is the angle defined in Equation (5.2).

In Figures 5.4 and 5.5, the average values of $p\!\!\!/_{\mathrm{T}}^{||,\mathrm{LJ}}$, $\langle p\!\!\!/_{\mathrm{T}}^{||,\mathrm{LJ}} \rangle$, are shown as a function of event centrality for four track p_{T} bins. The distributions in Figure 5.4 do not exhibit any centrality dependence while the distributions in Figure 5.5 do exhibit a small but significant residual centrality dependence even after the corrections discussed in Section 4.3. The overall magnitude of the missing p_{T} projection in the case of reconstructed events is also significantly smaller than in the case of truth. This is due to the combination of the deterioration of the missing p_{T} resolution, jet energy resolution, and tracking efficiency. Thus, this residual centrality dependence was corrected in each track-p_{T} interval and centrality interval separately by applying an additive correction derived as a difference of respective distributions in Figures 5.4 and 5.5. This correction was applied when the projections were calculated in the event loop. This procedure represents a simple bin-by-bin unfolding of reconstructed observable to the truth level. The resulting corrected distributions are shown in Figure 5.6. One can see a very good agreement of distributions between Figures 5.4 and 5.6.
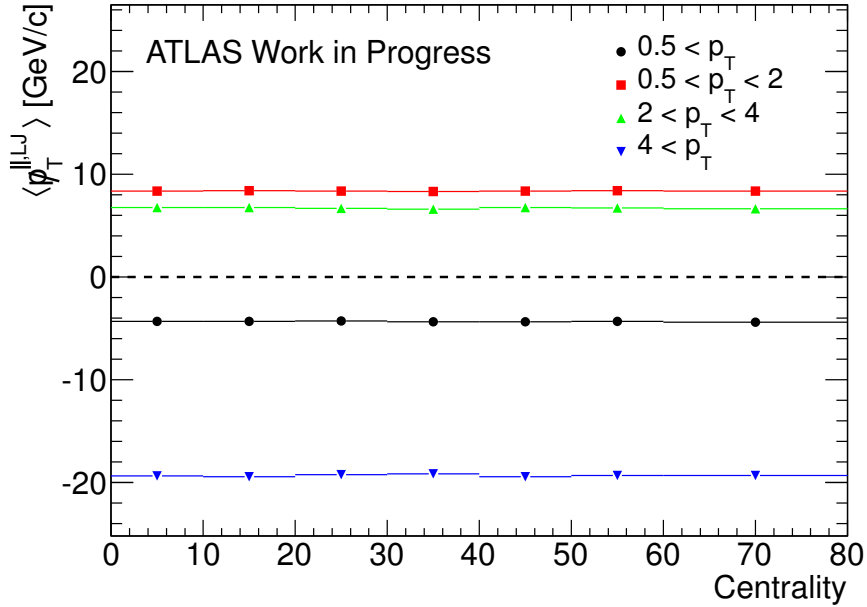

Figure 5.4: Average missing transverse momentum, $\langle p\!\!\!/_{\mathrm{T}}^{||,\mathrm{LJ}} \rangle$, projected onto the leading jet axis for four individual track p_{T} ranges in Truth MC. The $\langle p\!\!\!/_{\mathrm{T}}^{||,\mathrm{LJ}} \rangle$ values are shown as a function of collision centrality. The statistical uncertainty is smaller than the marker size and horizontal error bars represent a size of a given collision centrality bin.
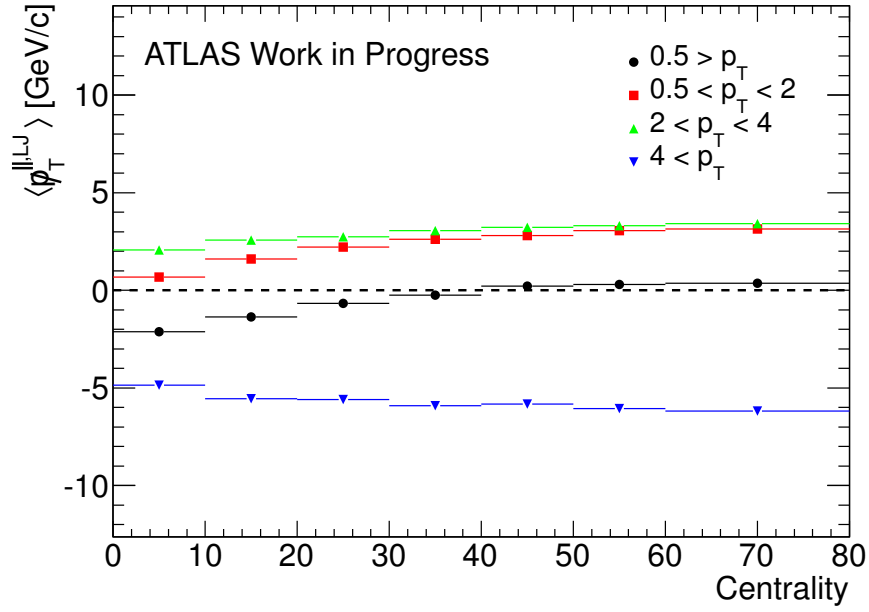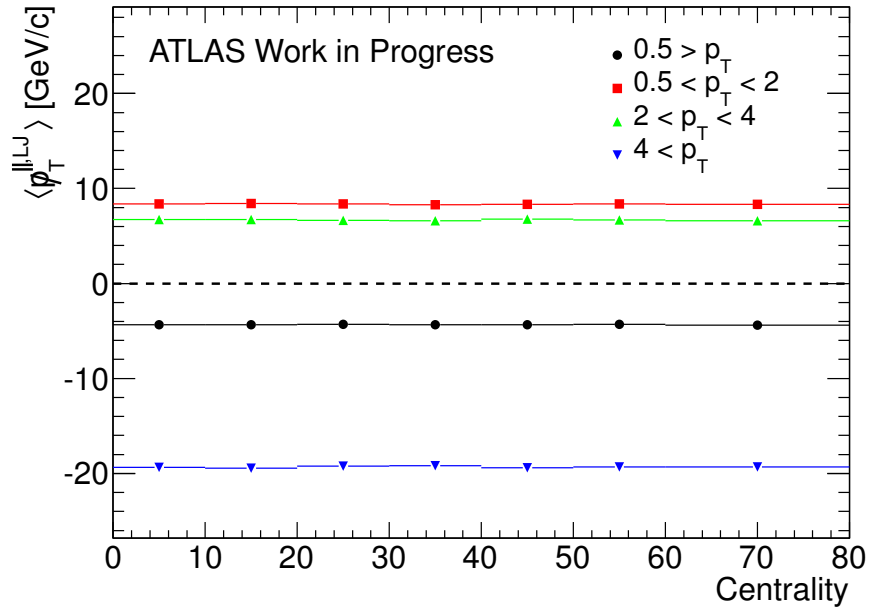
Figure 5.5: Average missing transverse momentum, $\langle \not{p}_T^{\|,\mathrm{LJ}} \rangle$, projected onto the leading jet axis for four individual track p_T ranges in reconstructed MC. The $\langle \not{p}_T^{\|,\mathrm{LJ}} \rangle$ values are shown as a function of collision centrality. The statistical uncertainty is smaller than the marker size and horizontal error bars represent a size of a given collision centrality bin.

Figure 5.6: Average missing transverse momentum, $\langle \not{p}_T^{\|,\mathrm{LJ}} \rangle$, projected onto the leading jet axis for four individual track p_T ranges in reconstructed MC after the unfolding. The $\langle \not{p}_T^{\|,\mathrm{LJ}} \rangle$ values are shown as a function of collision centrality. The statistical uncertainty is smaller than the marker size and horizontal error bars represent a size of a given collision centrality bin.

Figures 5.7 and 5.8 show the distributions of $p_T^{||,LJ}$ for both truth and reconstructed MC. One can see that for the truth MC the distributions are identical in all centrality bins. This is the same behavior as observed for the case of angles α_{LJ} in truth events. The reconstructed distributions are centrality dependent. They are more broad for central compared to peripheral collisions which reflects the fact that missing p_T resolution is deteriorated in central compared to peripheral collisions (as shown in Sections 4.2.1 or 4.3.2).
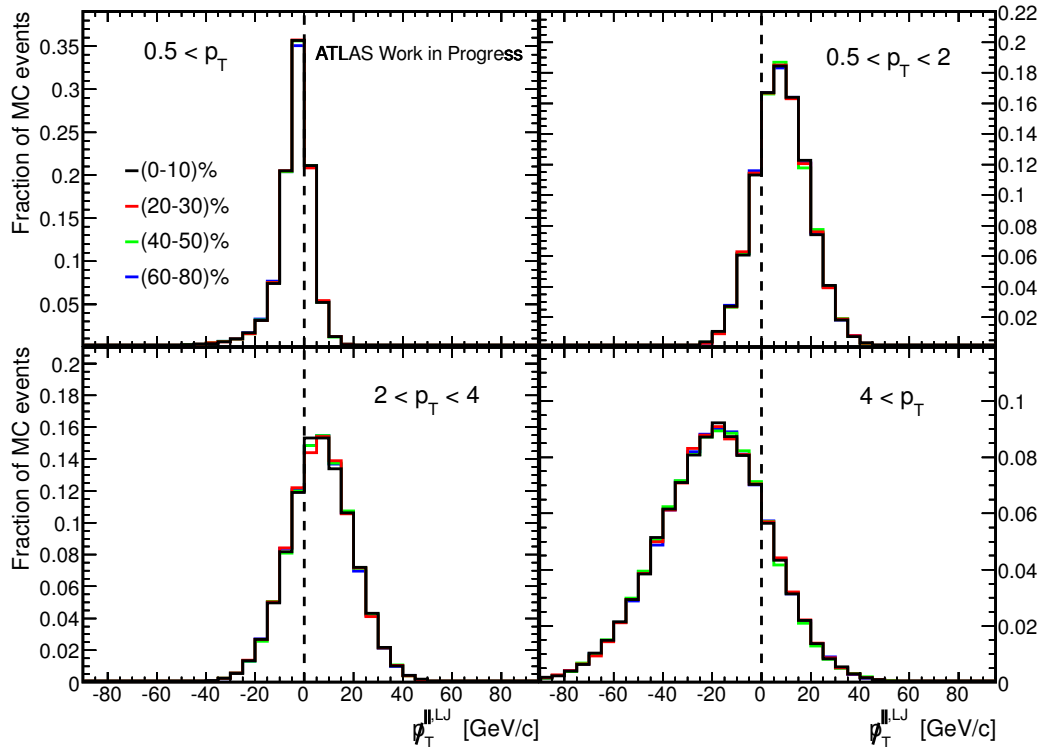
Figure 5.7: Probability distributions of the scalar projection of the p_T vector on the leading jet axis for four individual p_T ranges for truth Monte Carlo events.

Figures 5.9 and 5.10 present the average values of the projections as a function of dijet asymmetry, A_J, for four centrality bins ranging from $0 - 10\%$ to $50 - 80\%$. These figures show the average missing transverse momentum for tracks with $p_T > 0.5 \ \text{GeV/c}$, projected onto leading jet axis, as solid black circles. Colored boxes show the contributions to the mean p_T projection for three transverse momentum ranges from $0.5 - 2 \ \text{GeV/c}$ (blue) to $p_T > 4 \ \text{GeV/c}$ (red). For each panel $\langle p_T^{||,LJ} \rangle$ values are shown as a function of dijet asymmetry from almost balanced ($A_J < 0.1$) to unbalanced ($A_J > 0.5$) dijets. Following the definition of $p_T^{||,LJ}$, negative values represent an excess of particles in the direction of leading jet, while positive values indicate an excess of particles in the direction of subleading jet.

One can see from these plots that the magnitude of the $p_T^{||,LJ}$ to the leading jet axis increases with increasing asymmetry as one would expect – the events with large intrinsic A_J will tend to have large contribution of missing
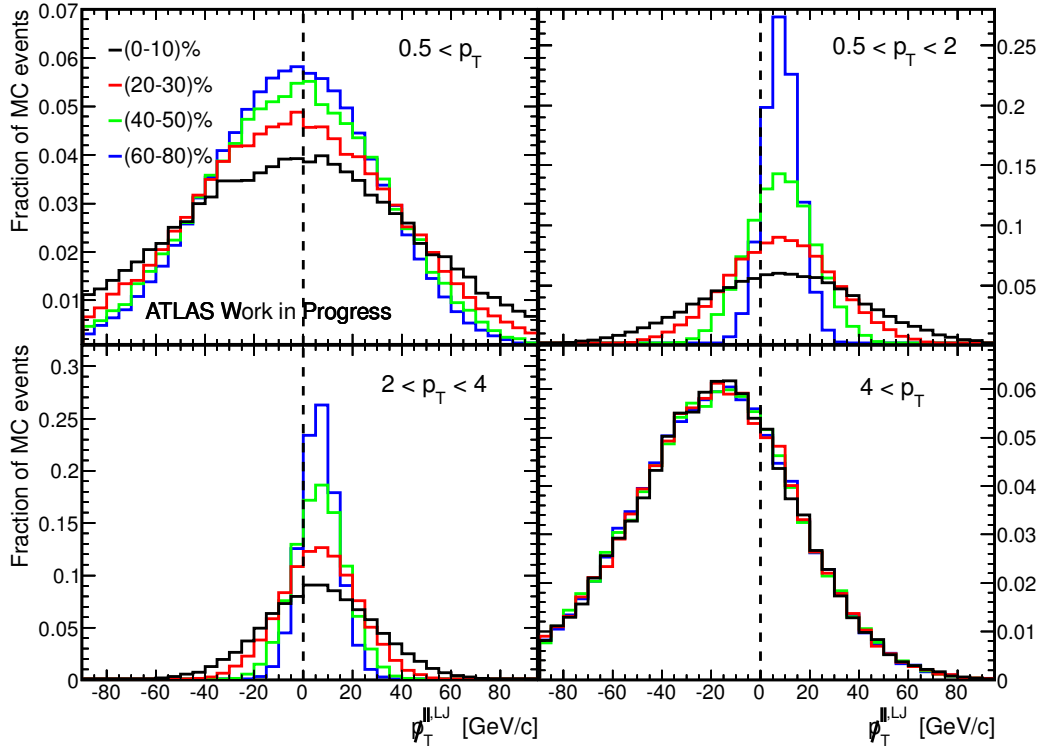
Figure 5.8: Probability distributions of the scalar projection of the $\not{p}_T$ vector on the leading jet axis for four individual p_T ranges for reconstructed Monte Carlo.

p_T pointing towards the subleading jet for hard particles ($p_T > 4$ GeV/c) and large contribution of missing p_T pointing towards a leading jet for soft particles ($0.5 < p_T < 2$ GeV). This can be seen both at the truth level and reconstructed level.

It is still possible to see some small residual differences between Figures 5.9 and 5.10 which means that the correction of the missing p_T projections to the truth level (unfolding) does not fully correct the missing p_T projections evaluated differentially in both the centrality and A_J. The goal of this analysis is not to provide all the observables corrected to the truth level but rather to quantify the energy flow and try to verify the observations by CMS. To achieve this goal it turns out that the unfolding of all the observables to the truth level is not needed and thus goes beyond the scope of this thesis. The important distributions prior applying the unfolding are summarized in Appendix A. One can see from the figures presented in the Appendix A that the physics conclusions discussed later in this Chapter do not change if the unfolding of the missing p_T projections is not performed.
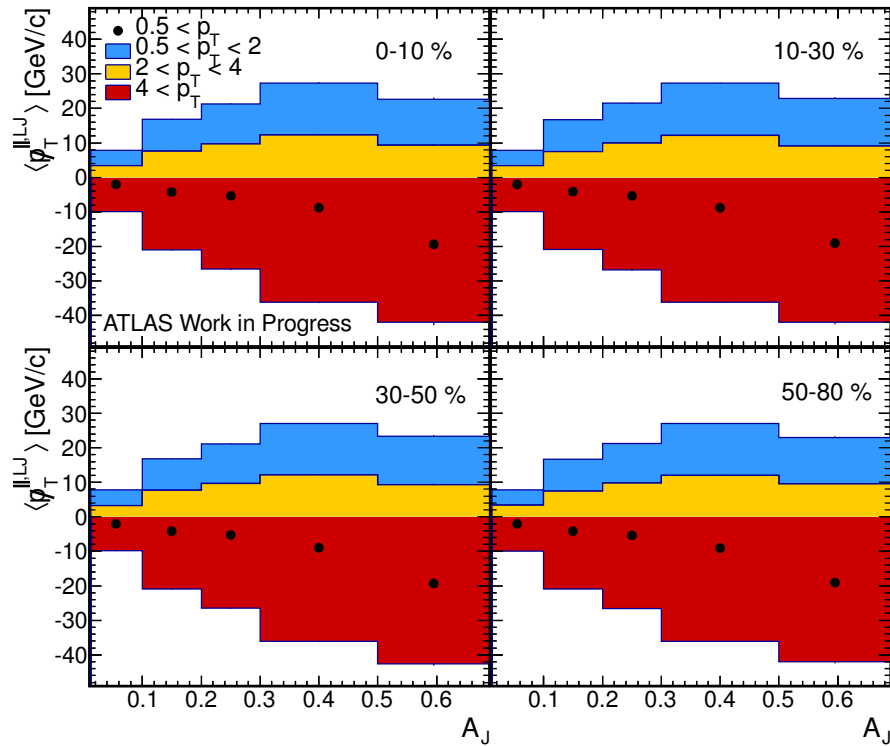
Figure 5.9: Average missing transverse momentum, $\langle \not{p}_{\mathrm{T}}^{\parallel,\mathrm{LJ}} \rangle$, projected onto the leading jet axis for four individual track p_{T} ranges shown as a function of A_{J} for four centrality bins in truth MC. The statistical errors are shown as vertical bars. Note that the blue and yellow histograms are "stacked" on top of each other.
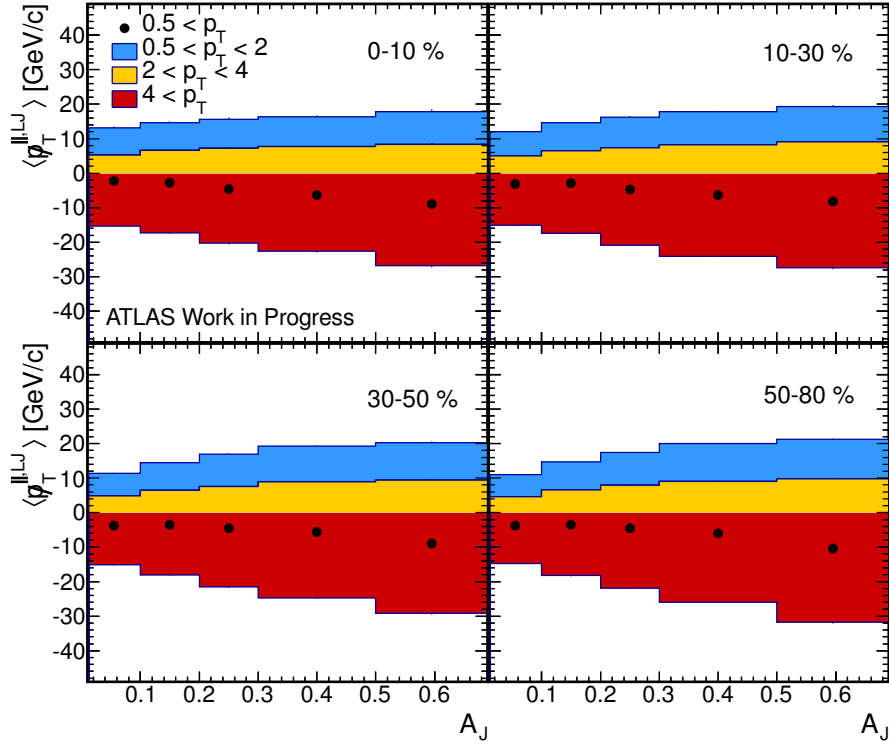
Figure 5.10: Average missing transverse momentum, $\langle \not{p}_{\mathrm{T}}^{\|,\mathrm{LJ}} \rangle$, projected onto the leading jet axis for four individual track p_{T} ranges shown as a function of A_{J} for four centrality bins in reconstructed MC. The statistical errors are shown as vertical bars. Note that the blue and yellow histograms are "stacked" on top of each other.

5.3 Analysis of Collision Data Sample

In this section we will present the same observables as those presented in Section 5.2, but reconstructed in real data. For the analysis presented in this section the hard-probe stream defined in Section 4.1.1 was used. The basic properties of corrections and missing pt distributions were cross-checked in the Minimum Bias stream as well. The plots of distributions of angle α_{LJ} are displayed in Figure . The scalar projections of $\not{p}_{\mathrm{T}}$ vector on leading jet axis (according to Equation (5.2)) are shown in Figure 5.12. Finally, the mean values of the distributions of these projections are displayed as a function of centrality in Figure 5.13 and as a function of dijet asymmetry A_{J} in Figure 5.14. Important differences in these distributions between the MC and real data are discussed in the next section.
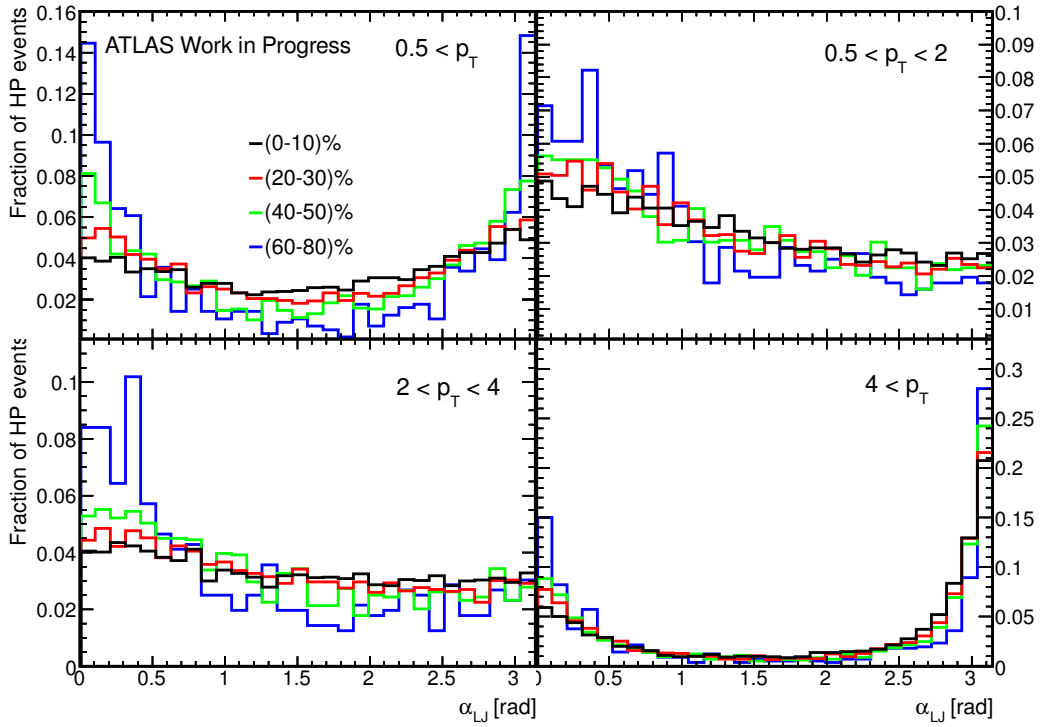
Figure 5.11: Probability distributions of the angle between the $\not{p}_T$ vector and leading jet axis for four individual p_T ranges.
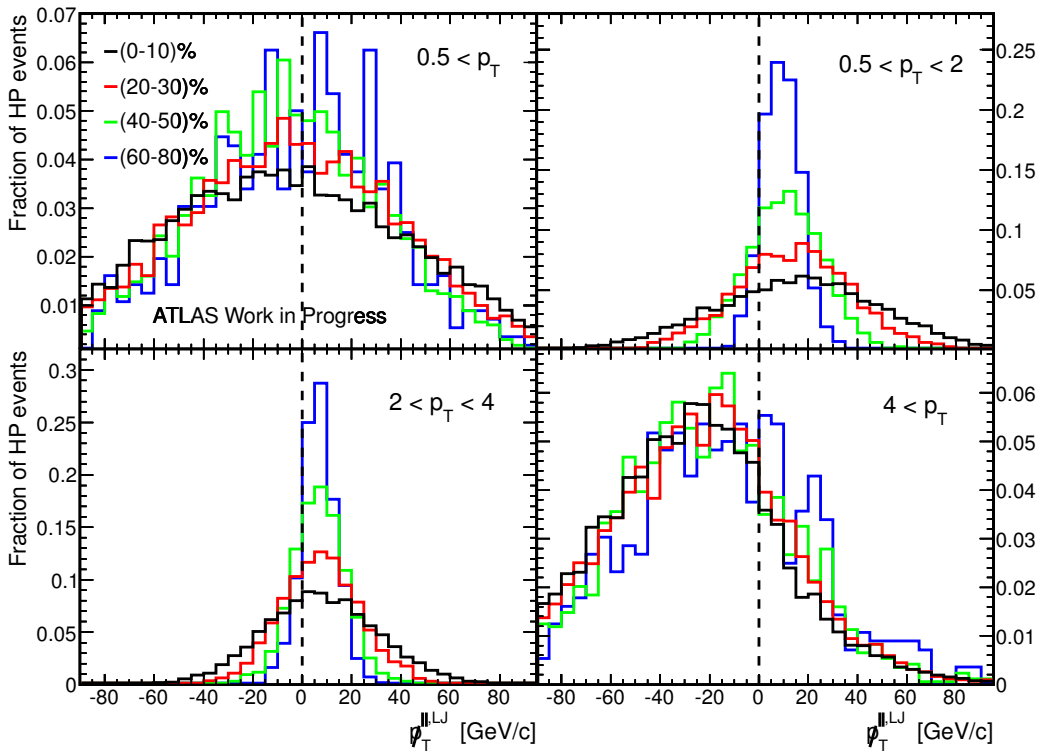

Figure 5.12: Probability distributions of the scalar projection of the $\not{p}_T$ vector on a leading jet axis for four individual p_T ranges.
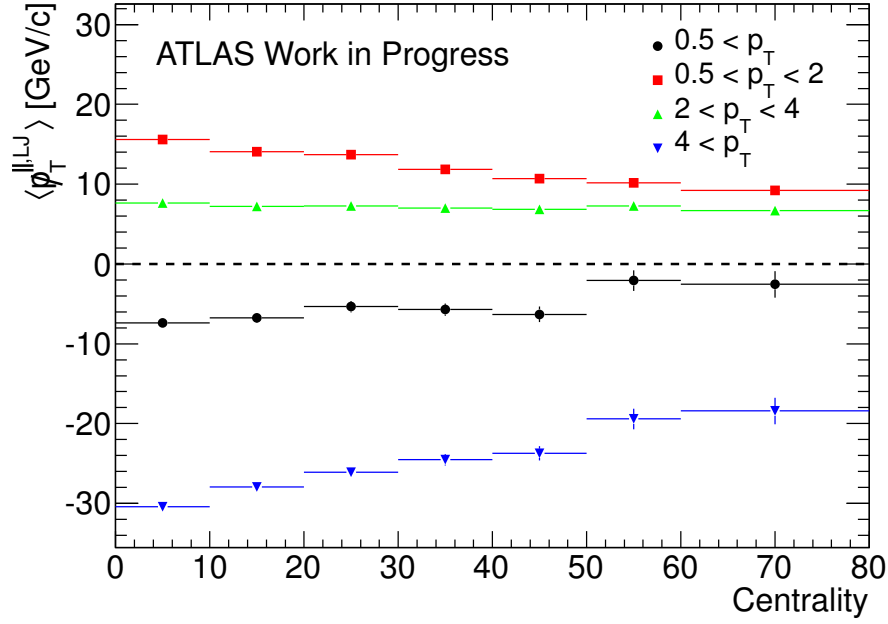
Figure 5.13: Average missing transverse momentum, $\langle p\!\!\!/_{\mathrm{T}}^{\|,\mathrm{LJ}} \rangle$, projected onto the leading jet axis for four individual track p_{T} ranges. The $\langle p\!\!\!/_{\mathrm{T}}^{\|,\mathrm{LJ}} \rangle$ values are shown as a function of collision centrality. Vertical error bars represent the statistical uncertainties and horizontal error bars represent a size of a given collision centrality bin.

5.4   Discussion

The most striking difference between the Monte Carlo and data results can be seen by comparing Figure 5.6 for reconstructed MC and Figure 5.13 for data. In the latter figure we can see that with the increasing centrality (centrality going to zero) the size of the $p\!\!\!/_{\mathrm{T}}$ projection calculated using the highest p_{T} particles increases towards negative values, which means an excess of yield of these high-p_{T} particles pointing towards the leading jet ($p\!\!\!/_{\mathrm{T}}$ points in the direction of the subleading jet). This means that more hard particles are in the leading jet than in the subleading jet. This excess is compensated by an excess of $p\!\!\!/_{\mathrm{T}}$ calculated using soft particles ($0.5\,\mathrm{GeV/c} < p_{\mathrm{T}} < 2\,\mathrm{GeV/c}$). This means that there are more soft particles in the subleading jet region. No such centrality dependence is observed in the equivalent plot for both truth, as well as reconstructed Monte Carlo. The underlying physics picture is following: in central collisions the subleading jet is very often strongly quenched, which means that the yield of hard particles is suppressed. The energy from these hard particles is transferred to soft particles, which show an enhanced yield in central collisions.

This physics picture can be concluded also from the plots in Figure 5.14, which evaluate the mean missing p_{T} projection as a function of dijet asymmetry separately for four centrality ranges ranging from central ($0-10\%$) to peripheral ($50-80\%$) collisions. With increasing asymmetry the imbalance increases and
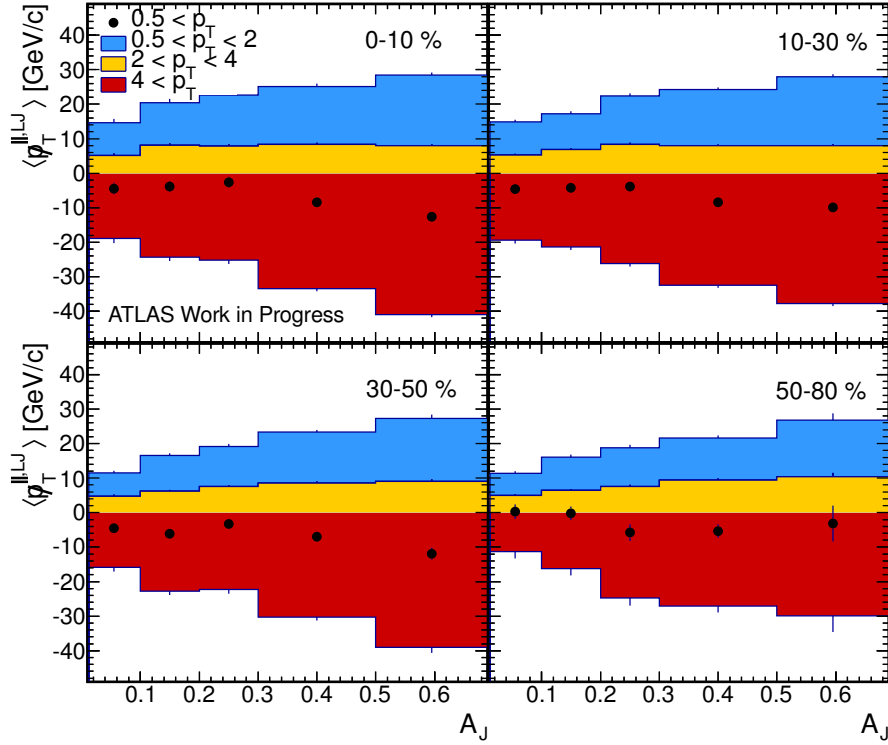
Figure 5.14: Average missing transverse momentum, $\langle \displaystyle{\not}p_{\mathrm{T}}^{\|,\mathrm{LJ}} \rangle$, projected onto the leading jet axis for four individual track p_{T} ranges shown as a function of A_{J} for four centrality bins. The statistical errors are shown as vertical bars. Note that the blue and yellow histograms are "stacked" on top of each other.

the lack of the high-p_{T} particles in the subleading jet (negative values of $\displaystyle{\not}p_{\mathrm{T}}^{\|,\mathrm{LJ}}$ in Figure 5.14) is compensated by the excess of softer particles in the region of $0.5 - 4\ \mathrm{GeV/c}$ (positive values of $\displaystyle{\not}p_{\mathrm{T}}^{\|,\mathrm{LJ}}$ in Figure 5.14), as expected. In peripheral PbPb collisions and for all centrality selections of MC, this excess of hard particles in leading jet is compensated by both intermediate p_{T} particles from $2 - 4\ \mathrm{GeV/c}$ and soft p_{T} particles between $0.5 - 2\ \mathrm{GeV/c}$ with approximately equal contributions. As we move towards more central PbPb collisions, however, the balancing contribution of soft particles is significantly larger than the contribution from intermediate p_{T} particles. This is consistent with the picture of medium-induced energy loss mechanism resulting in a softer spectrum of charged particles. This effect is strongest for large A_{J} dijets observed in central PbPb collisions, where the size of hot, dense medium is expected to be largest resulting in most significant quenching effects.

One also observes that generally, the total projected momenta in the events, shown as solid markers in Figures 5.14 and 5.10, are found to be balanced to maximum value of $\displaystyle{\not}p_{\mathrm{T}}^{\|,\mathrm{LJ}}$ of approximately $12\ \mathrm{GeV/c}$ for events with the largest A_{J}. This trend can be observed in both truth, as well as reconstructed PYTHIA MC events. The reason for this deviation from zero can be the transverse momentum threshold of $0.5\ \mathrm{GeV/c}$ imposed on charged particles or the acceptance

of the tracker.

In order to draw more quantitative conclusions we have evaluated the differences between the reconstructed distributions in MC and real data. The best way to do so is to show the difference between the contributions of different track p_T ranges to $\langle \not{p}_T^{\|,LJ} \rangle$ in PbPb data and reconstructed Monte Carlo. This final result is shown in Figure 5.15. While the contributions from the various p_T ranges for PbPb data and MC are similar for peripheral collisions, a difference can be seen for central collisions, with a significant excess of soft charged particles for asymmetric jets in PbPb collisions.
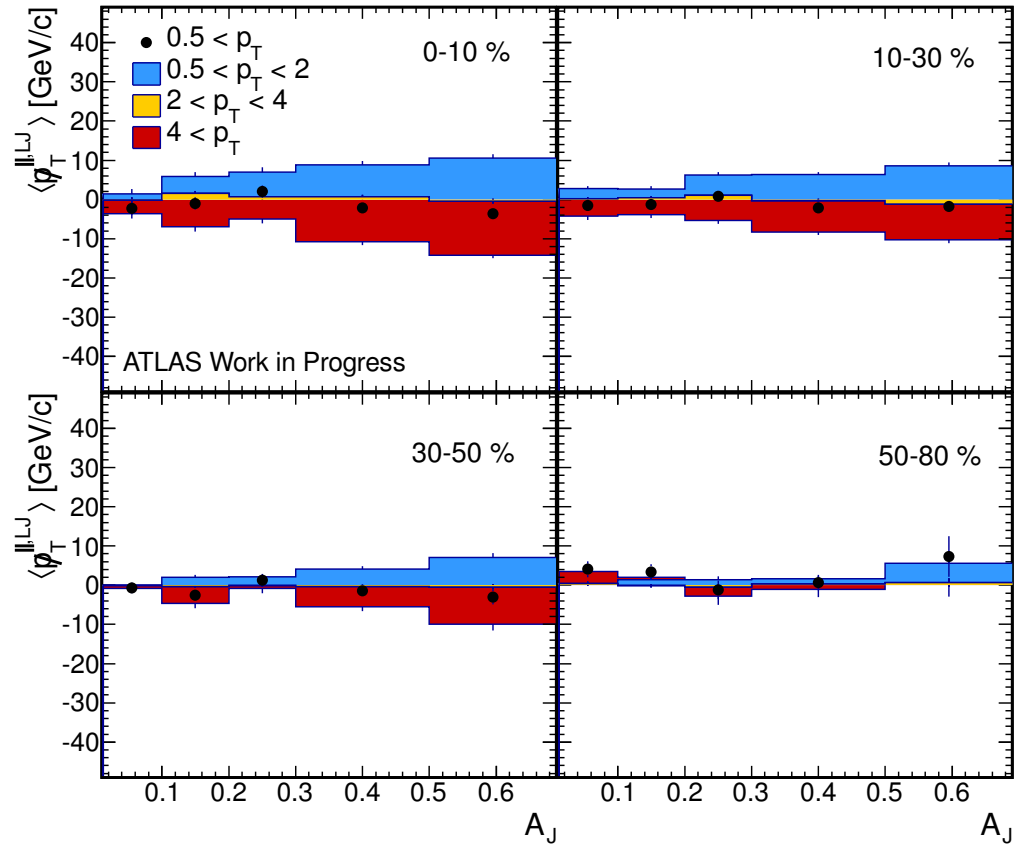

Figure 5.15: Difference (PbPb Data - PbPb Reconstructed MC) of the $\langle \not{p}_T^{\|,LJ} \rangle$ evaluated as a function of dijet asymmetry for the individual momentum ranges of charged particles.

5.4.1 Comparison with the CMS study

These results, especially those displayed in Figures 5.14 and 5.15, can be compared with the results obtained by CMS Collaboration, published in [22]. We should note that there are some small differences between the analysis of CMS and the analysis in this work. Namely there is a difference in the jet selection requirements – CMS uses following: $E_{T1} > 120$ GeV, $E_{T2} > 50$ GeV, $\Delta\phi > 5/6\pi$, while in this analysis we use: $E_{T1} > 100$ GeV, $E_{T2} > 25$ GeV, $\Delta\phi > 2/3\pi$ which were adopted from the original paper [35].

Of the main interest are the figures shown in the bottom row of Figure 5.16. It is possible to directly compare these figures with Figure 5.15 presented in previous section. As we can see, both of these figures exhibit a very good correspondence between each other and we can therefore conclude that we have confirmed the observation done previously by the CMS Collaboration.
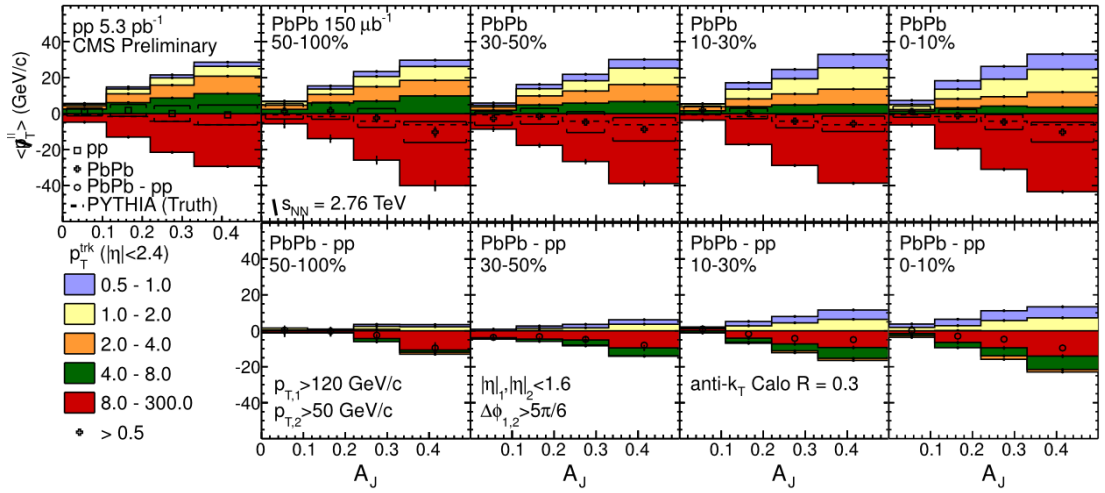

Figure 5.16: (Upper row) Average missing transverse momentum, $\langle \not{p}_T^{||,LJ} \rangle$, for pp collisions (left) and four selections of PbPb collision centrality ranging from $50 - 100\%$ to $0 - 10\%$. The solid markers show $\langle \not{p}_T^{||,LJ} \rangle$ averaged over all tracks with $p_T > 0.5$ GeV/c, while the colored boxes show the contribution to $\langle \not{p}_T^{||,LJ} \rangle$ for various momentum ranges from $0.5 < p_T < 1$ GeV/c (light blue) to $p_T > 8$ GeV/c (red). For the solid circles, vertical bars and brackets represent the statistical and systematic uncertainties, respectively. For the individual p_T ranges, the statistical uncertainties are shown as vertical bars. (Lower row) Difference PbPb - pp of the $\langle \not{p}_T^{||,LJ} \rangle$ contribution for the individual momentum ranges shown in the upper panel. Error bars and brackets represent statistical and systematic uncertainties respectively.

Summary and Conclusions

In this work, the data collected by ATLAS detector have been used to investigate the behavior of missing transverse momentum in PbPb collisions at center-of-mass energy $\sqrt{s_{\mathrm{NN}}} = 2.76$ TeV. Before the analysis of the data produced by ATLAS a simple "toy" MC simulation has been performed to study the basic mechanism of $\not{p}_{\mathrm{T}}$ production.

We analyzed two samples of collision data and corresponding MC simulation. The first of the collision data samples was the minimum bias data sample, corresponding to an integrated luminosity of 0.7 $\mu\mathrm{b}^{-1}$, which has been used to define the collision centrality. These data were also used to investigate and construct the corrections for the x and y components of the missing transverse momentum vector. These corrections had to be applied in order to compensate for the faulty parts of the ID tracking system.

The second data sample, a jet data sample, has been used to study the flow of the energy missing in the subleading jet. Jets were reconstructed using the anti-k_t jet clustering algorithm with the distance parameter of $R = 0.4$ in a data sample corresponding to an integrated luminosity of 140 $\mu\mathrm{b}^{-1}$. Only events with $|\eta| < 2.1$ having leading and subleading jet energies higher than 100 GeV and 25 GeV, respectively, were selected. Only the tracks with $p_{\mathrm{T}} > 0.5$ GeV/c were used in this study. The p_{T} of tracks was corrected to compensate for the inefficiency of the ID tracking system. Jets were corrected by standard corrections used by ATLAS.

The momentum flow in PbPb and MC events containing high momentum jets has been studied and it was shown that for a given dijet asymmetry, the dijet momentum imbalance in PbPb is found to be compensated by particles at lower transverse momentum ($p_{\mathrm{T}} = 0.5 - 2$ GeV/c) compared to the PYTHIA simulated collisions, where most of the momentum balance is found in the higher transverse momentum range ($p_{\mathrm{T}} = 2 - 4$ GeV/c). These measurements show an increasing difference between PbPb and MC for more central collisions, reflecting a softening of the charged particle spectra carrying the momentum balance of asymmetric dijet systems.

All things considered, these results should provide an important qualitative and quantitative insight into the transport properties of the medium created in heavy-ion collisions. Furthermore, the results are in a very good agreement with previously published results by CMS [22].

Bibliography

[1] K. Yagi, T. Hatsuda, and Y. Miake. *Quark-gluon plasma: From big bang to little bang*, volume 23. 2005.

[2] F. Halzen and Alan D. Martin. *Quarks and leptons: An introductory course in moder particle physics*. 1984.

[3] Michael E. Peskin and Daniel V. Schroeder. *An Introduction to quantum field theory*. 1995.

[4] M. Munowitz. *Knowing: The nature of physical law*. 2005.

[5] David J. Gross and Frank Wilczek. Ultraviolet Behavior of Nonabelian Gauge Theories. *Phys.Rev.Lett.*, 30:1343–1346, 1973.

[6] H. David Politzer. Reliable Perturbative Results for Strong Interactions? *Phys.Rev.Lett.*, 30:1346–1349, 1973.

[7] Vernon D. Barger and R.J.N. Phillips. Collider Physics. 1987.

[8] Siegfried Bethke. Experimental tests of asymptotic freedom. *Prog.Part.Nucl.Phys.*, 58:351–386, 2007.

[9] Berndt Muller. *The Physics of the Quark-Gluon Plasma*, volume 225. 1985.

[10] Mikhail A. Stephanov. QCD phase diagram and the critical point. *Prog.Theor.Phys.Suppl.*, 153:139–156, 2004.

[11] Mark G. Alford, Andreas Schmitt, Krishna Rajagopal, and Thomas Schäfer. Color superconductivity in dense quark matter. *Rev.Mod.Phys.*, 80:1455–1515, 2008.

[12] Misha A. Stephanov, K. Rajagopal, and Edward V. Shuryak. Signatures of the tricritical point in QCD. *Phys.Rev.Lett.*, 81:4816–4819, 1998.

[13] Krishna Rajagopal and Frank Wilczek. The Condensed matter physics of QCD. 2000.

[14] Peter Jacobs and Xin-Nian Wang. Matter in extremis: Ultrarelativistic nuclear collisions at RHIC. *Prog.Part.Nucl.Phys.*, 54:443–534, 2005.

[15] J.D. Bjorken. Energy Loss of Energetic Partons in Quark - Gluon Plasma: Possible Extinction of High p_T Jets in Hadron - Hadron Collisions. 1982.

[16] L.P. Csernai. *Introduction to relativistic heavy ion collisions*. 1994.

[17] Ramona Vogt. *Ultrarelativistic heavy-ion collisions*. 2007.

[18] Raimond Snellings. Elliptic Flow: A Brief Review. *New J.Phys.*, 13:055008, 2011.

[19] Roy J. Glauber. Quantum Optics and Heavy Ion Physics. *Nucl.Phys.*, A774:3–13, 2006.

[20] Prashant Shukla. The Glauber model and the heavy ion reaction cross-section. *Phys.Rev.*, C67:054607, 2003.

[21] Michael L. Miller, Klaus Reygers, Stephen J. Sanders, and Peter Steinberg. Glauber modeling in high energy nuclear collisions. *Ann.Rev.Nucl.Part.Sci.*, 57:205–243, 2007.

[22] Serguei Chatrchyan et al. Observation and studies of jet quenching in PbPb collisions at nucleon-nucleon center-of-mass energy = 2.76 TeV. *Phys.Rev.*, C84:024906, 2011.

[23] Georges Aad et al. Measurements of the Nuclear Modification Factor for Jets in Pb+Pb Collisions at $\sqrt{s_\mathrm{NN}} = 2.76$ TeV with the ATLAS Detector. *Phys.Rev.Lett.*, 114(7):072302, 2015.

[24] John B. Kogut and Leonard Susskind. Vacuum Polarization and the Absence of Free Quarks in Four-Dimensions. *Phys.Rev.*, D9:3501–3512, 1974.

[25] Yuri L. Dokshitzer, Valery A. Khoze, Alfred H. Mueller, and S.I. Troian. Basics of perturbative QCD. 1991.

[26] André Mischke. Research. `http://www.staff.science.uu.nl/~misch101/research.htm`. [Online; accessed 24-February-2015].

[27] S. Catani, Yu.L. Dokshitzer, M. Olsson, G. Turnock, and B.R. Webber. New clustering algorithm for multijet cross sections in e+e- annihilation. *Physics Letters B*, 269(3–4):432 – 438, 1991.

[28] S. Catani, Yu.L. Dokshitzer, M.H. Seymour, and B.R. Webber. Longitudinally-invariant kt-clustering algorithms for hadron-hadron collisions. *Nuclear Physics B*, 406(1–2):187 – 224, 1993.

[29] G. Aad et al. Expected Performance of the ATLAS Experiment - Detector, Trigger and Physics. 2009.

[30] Yuri L. Dokshitzer, G.D. Leder, S. Moretti, and B.R. Webber. Better jet clustering algorithms. *JHEP*, 9708:001, 1997.

[31] Matteo Cacciari, Gavin P. Salam, and Gregory Soyez. The Anti-k_t jet clustering algorithm. *JHEP*, 0804:063, 2008.

[32] Xin-Nian Wang and Miklos Gyulassy. Energy and centrality dependence of rapidity densities at RHIC. *Phys.Rev.Lett.*, 86:3496–3499, 2001.

[33] Xin-Nian Wang. pQCD based approach to parton production and equilibration in high-energy nuclear collisions. *Phys.Rept.*, 280:287–371, 1997.

[34] David d'Enterria. Jet quenching. *Landolt-Bornstein*, 23:471, 2010.

[35] Georges Aad et al. Observation of a Centrality-Dependent Dijet Asymmetry in Lead-Lead Collisions at $\sqrt{s_{NN}} = 2.77$ TeV with the ATLAS Detector at the LHC. *Phys.Rev.Lett.*, 105:252303, 2010.

[36] P.M. Jacobs and M. van Leeuwen. High p_T in nuclear collisions at SPS, RHIC, and LHC. *Nucl.Phys.*, A774:237–246, 2006.

[37] Measurement of transverse momentum flow relative to the dijet system in PbPb and pp collisions at $\sqrt{s_{NN}} = 2.76$ TeV. Technical Report CMS-PAS-HIN-14-010, CERN, Geneva, 2014.

[38] Lyndon Evans and Philip Bryant. LHC Machine. *JINST*, 3:S08001, 2008.

[39] Jean-Luc Caron. Overall view of LHC experiments.. Vue d'ensemble des experiences du LHC. AC Collection. Legacy of AC. Pictures from 1992 to 2002., May 1998.

[40] A. Beuret, A. Blas, J. Borburgh, H. Burkhardt, C. Carli, et al. The LHC Lead Ion Injector Chain. 2004.

[41] G. Aad et al. The ATLAS Experiment at the CERN Large Hadron Collider. *JINST*, 3:S08003, 2008.

[42] Atlas experiment. `http://www.atlas.ch/detector.html`. [Online; accessed 24-February-2015].

[43] J. Beringer et al. Review of Particle Physics (RPP). *Phys.Rev.*, D86:010001, 2012.

[44] A.R. Baden. Jets and kinematics in hadronic collisions. *Int.J.Mod.Phys.*, A13:1817–1845, 1998.

[45] C. Adler et al. Pion interferometry of $\sqrt{s_{NN}} = 130$ GeV Au+Au collisions at RHIC. *Phys.Rev.Lett.*, 87:082301, 2001.

[46] Georges Aad et al. Measurement of underlying event characteristics using charged particles in pp collisions at $\sqrt{s} = 900$ GeV and 7 TeV with the ATLAS detector. *Phys.Rev.*, D83:112001, 2011.

[47] G. Aad et al. Charged-particle multiplicities in pp interactions at $\sqrt{s} = 900$ GeV measured with the ATLAS detector at the LHC. *Phys.Lett.*, B688:21–42, 2010.

[48] Georges Aad et al. Measurement of the pseudorapidity and transverse momentum dependence of the elliptic flow of charged particles in lead-lead collisions at $\sqrt{s_{NN}} = 2.76$ TeV with the ATLAS detector. *Phys.Lett.*, B707:330–348, 2012.

[49] Georges Aad et al. Measurement of inclusive jet charged-particle fragmentation functions in Pb+Pb collisions at $\sqrt{s_{NN}} = 2.76$ TeV with the ATLAS detector. *Phys.Lett.*, B739:320–342, 2014.

[50] S. Agostinelli et al. GEANT4: A Simulation toolkit. *Nucl.Instrum.Meth.*, A506:250–303, 2003.

[51] G. Aad et al. The ATLAS Simulation Infrastructure. *Eur.Phys.J.*, C70:823–874, 2010.

[52] Atlas internal communication. `https://twiki.cern.ch/twiki/bin/viewauth/AtlasProtected/HeavyIonAnalysis2011`. [Online; accessed 24-February-2015].

[53] Serguei Chatrchyan et al. Missing transverse energy performance of the CMS detector. *JINST*, 6:P09001, 2011.

Appendix A

Distributions Prior the Unfolding

In this appendix, we summarize the important distributions evaluated prior the unfolding described in Section 5.2. One can see that the unfolding of the missing p_{T} projections does not influence the overall conclusion of the analysis.
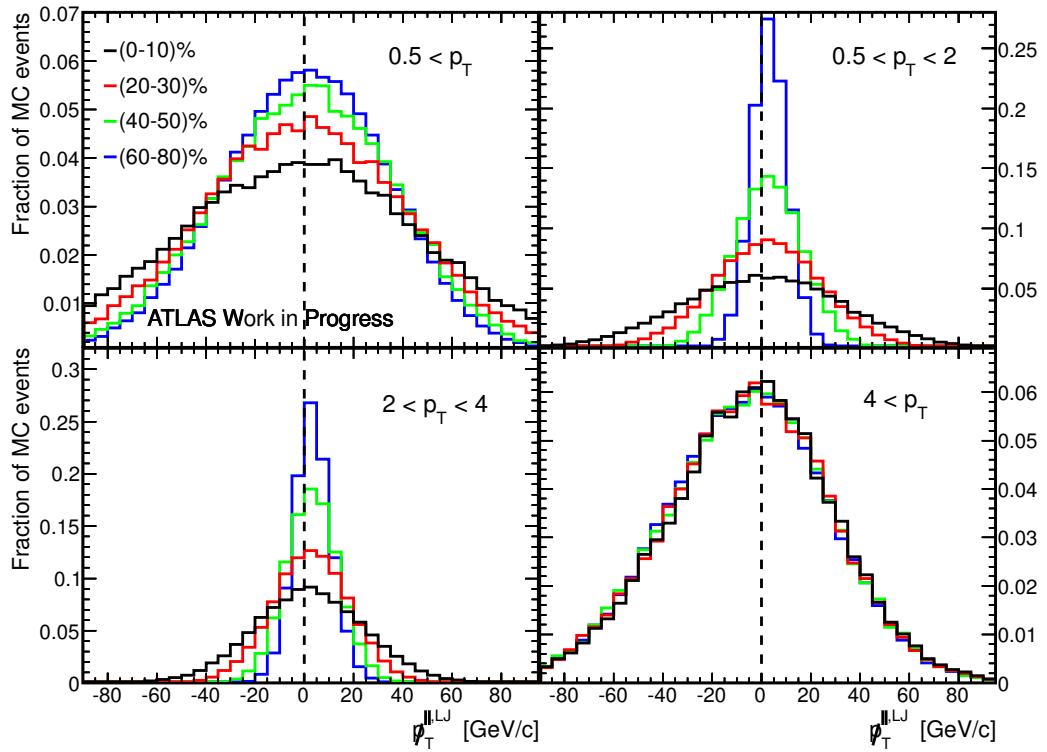

Figure A.1: Probability distributions of the scalar projection of the $\not{p}_{\mathrm{T}}$ vector on the leading jet axis for four individual p_{T} ranges for reconstructed Monte Carlo.
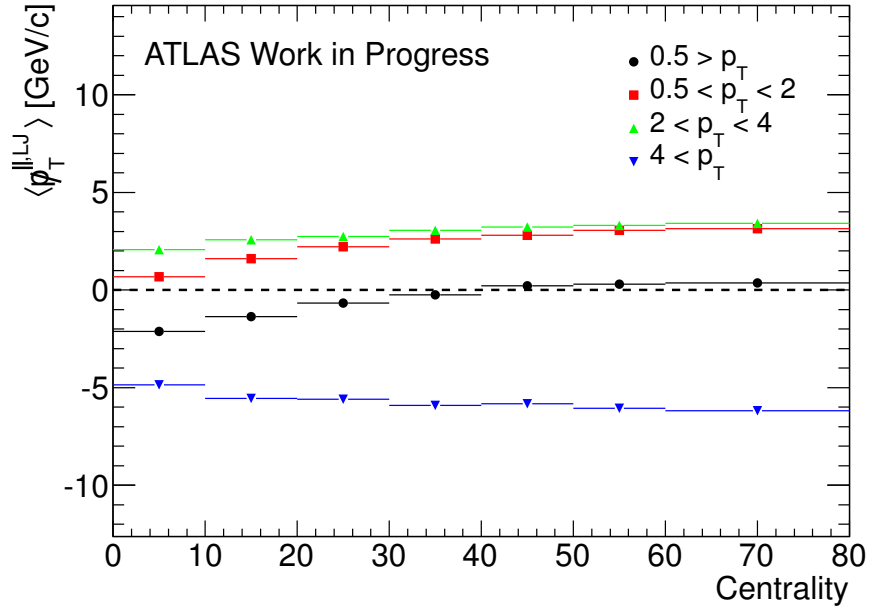
Figure A.2: Average missing transverse momentum, $\langle p_T^{\|,LJ} \rangle$, projected onto the leading jet axis for four individual track p_T ranges. The $\langle p_T^{\|,SJ} \rangle$ values are shown as a function of collision centrality. The statistical uncertainty is smaller than the marker size and horizontal represent a size of a given collision centrality bin. (Reconstructed Monte Carlo)
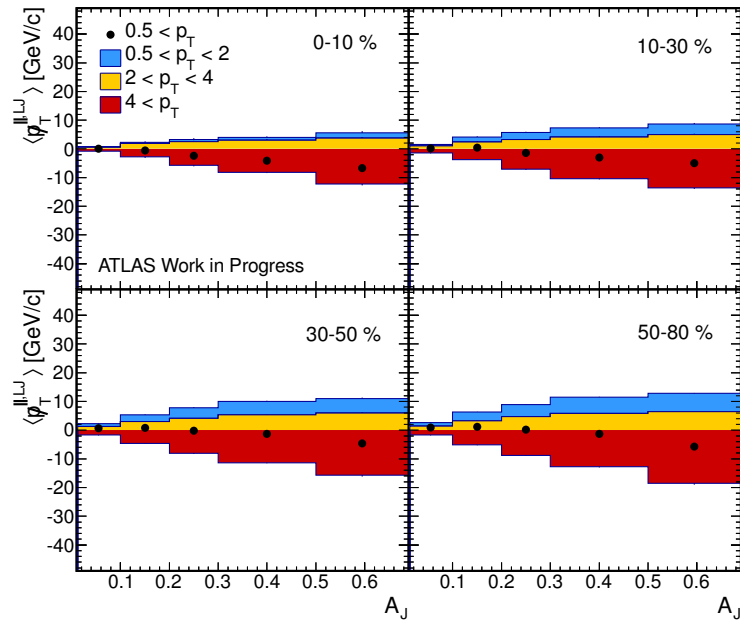

Figure A.3: Average missing transverse momentum, $\langle p_T^{\|,LJ} \rangle$, projected onto the leading jet axis for four individual track p_T ranges. The $\langle p_T^{\|,LJ} \rangle$ values are shown as a function of A_J for four centrality bins. The statistical errors are shown as vertical bars. Note that the blue and yellow histograms are "stacked" on top of each other. (Reconstructed Monte Carlo)
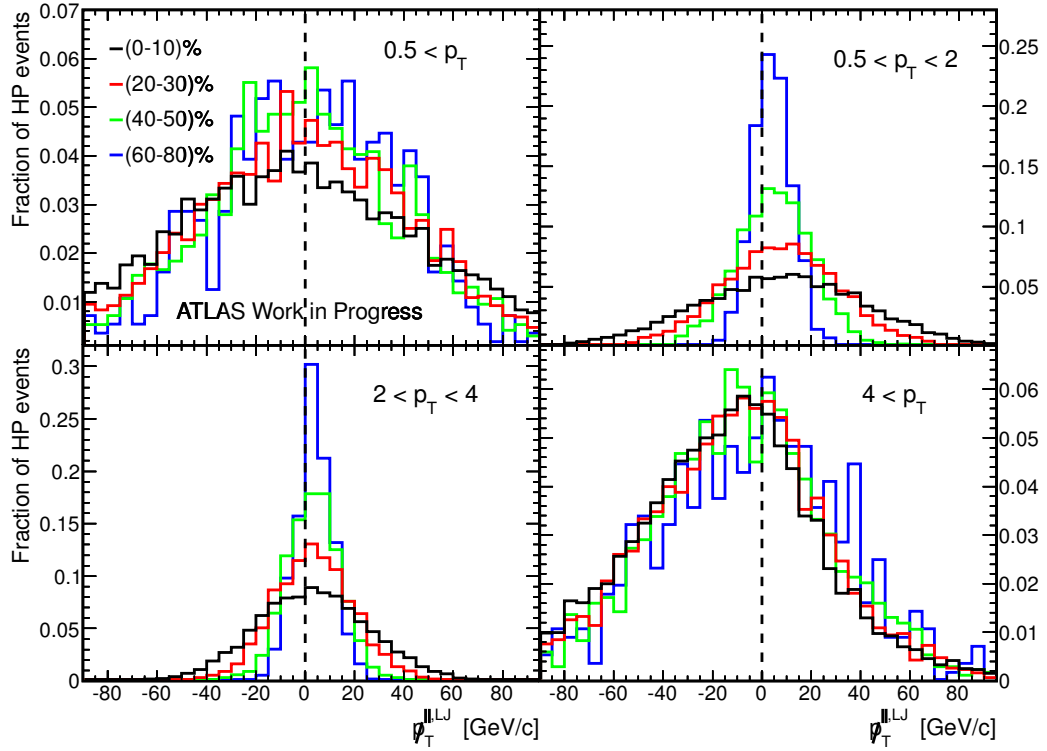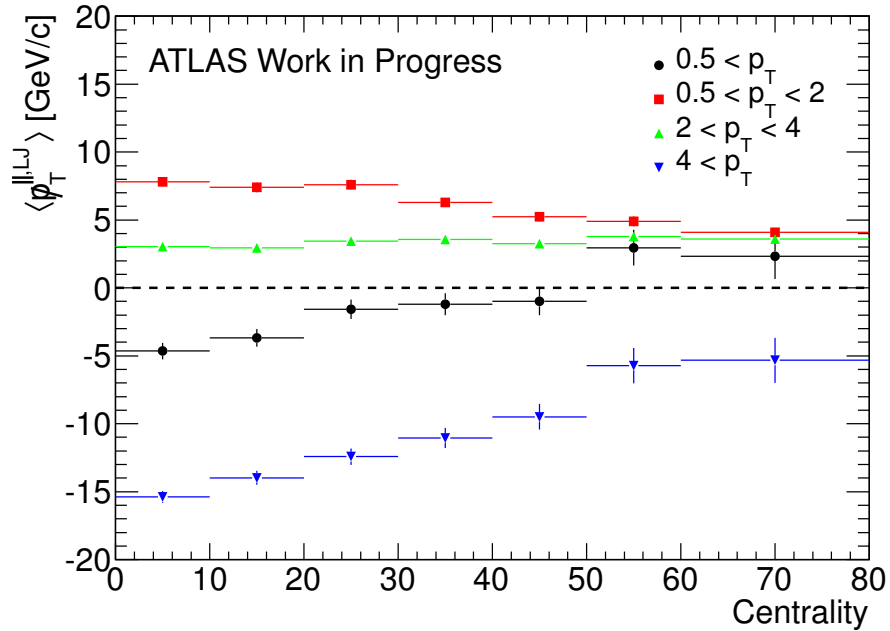
Figure A.4: Probability distributions of the scalar projection of the $\not{p}_T$ vector on a leading jet axis for four individual p_T ranges in real data.

Figure A.5: Average missing transverse momentum, $\langle \not{p}_T^{||,LJ} \rangle$, projected onto the leading jet axis for four individual track p_T ranges. The $\langle \not{p}_T^{||,LJ} \rangle$ values are shown as a function of collision centrality. Vertical error bars represent the statistical uncertainties and horizontal represent a size of a given collision centrality bin. (Data sample)
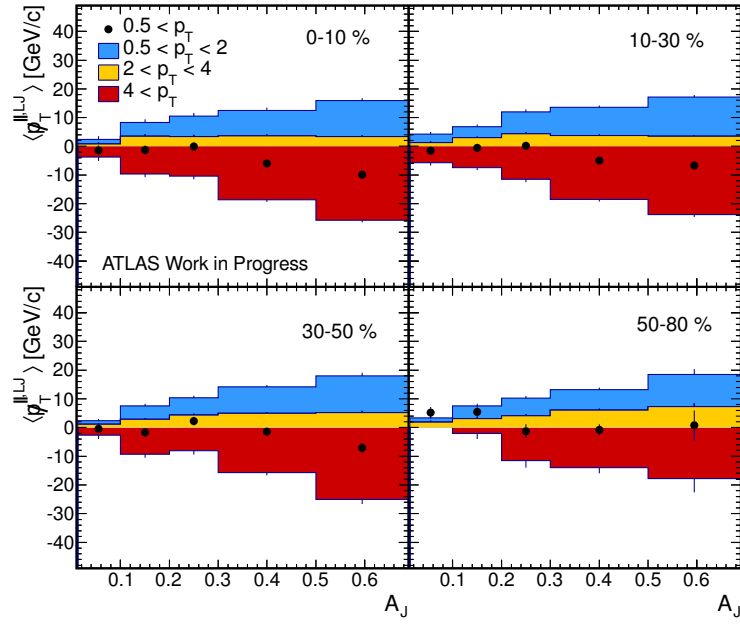
Figure A.6: Average missing transverse momentum, $\langle p_T^{||,\mathrm{LJ}} \rangle$, projected onto the leading jet axis for four individual track p_T ranges. The $\langle p_T^{||,\mathrm{LJ}} \rangle$ values are shown as a function of A_J for four centrality bins. The statistical errors are shown as vertical bars. Note that the blue and yellow histograms are "stacked" on top of each other. (Data sample)
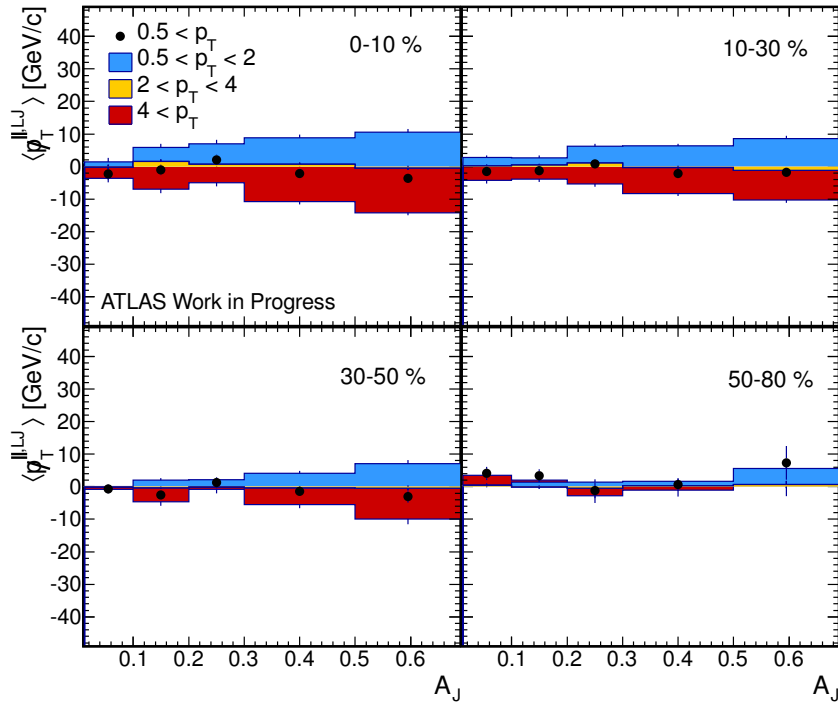

Figure A.7: Difference (PbPb Data - PbPb Reconstructed MC) of the $\langle p_T^{||,\mathrm{LJ}} \rangle$ evaluated as a function of dijet asymmetry for the individual momentum ranges of charged particles.